

# Auto-consistent metallicity and star formation history of the nearest blue compact dwarf galaxy NGC 6789

R. García-Benito<sup>1,2\*</sup> and E. Pérez-Montero<sup>2</sup>

<sup>1</sup>*Kavli Institute of Astronomy and Astrophysics, Peking University, 100871, Beijing, China*

<sup>2</sup>*Instituto de Astrofísica de Andalucía, CSIC, Apartado de correos 3004, 18080 Granada, Spain*

Accepted 2012 March 8

## ABSTRACT

We present a detailed auto-consistent study of the nearest blue compact dwarf galaxy NGC 6789 by means of optical and UV archive photometry data and optical long-slit ISIS-WHT spectroscopy observations of the five brightest star-forming knots. The analysis of the spectra in all knots allowed the derivation of ionic chemical abundances of oxygen, nitrogen, sulphur, argon and neon using measures of both the high- and low-excitation electron temperatures, leading to the conclusion that NGC 6789 is chemically homogeneous with low values of the abundance of oxygen in the range  $12+\log(\text{O}/\text{H}) = 7.80\text{--}7.93$ , but presenting at the same time higher values of the nitrogen-to-oxygen ratio than expected for its metal regime.

We used archival *Hubble Space Telescope*/Wide-Field Planetary Camera 2 (HST/WFPC2) F555W and F814W observations of NGC 6789 to perform a photometric study of the colour-magnitude diagram (CMD) of the resolved stellar populations and derive its star formation history (SFH), which is compatible with the presence of different young and old stellar populations whose metallicities do not necessarily increase with age. We fit the observed optical spectrum in all the five knots using the STARLIGHT code and a combination of single stellar populations following the SFH obtained from the CMD. We compare the resulting stellar masses and the relative fractions of the ionising populations with a non-constrained SFH case. The properties of the younger populations were obtained using CLOUDY photoionisation models, giving similar ages in all the knots in the range 3–6 Myr and the estimation of the dust absorption factor, which correlates with the observed GALEX FUV-NUV colour indices. The total photometric extinction and dust-absorption corrected H $\alpha$  fluxes were finally used to derive the star formation rates.

**Key words:** ISM: abundances – H II regions – galaxies: dwarf – galaxies: individual: NGC 6789 – galaxies: starburst – galaxies: star formation – Hertzsprung-Russell and colour-magnitude diagrams

## 1 INTRODUCTION

Blue compact dwarf galaxies (BCDs) are known by their intense processes of star-formation. These make that their optical spectra were dominated by the blue light from massive young stars and the bright emission lines from the ionised gas, so they are also called H II galaxies.

Their high specific star-formation rates and their low gas-phase metallicities were taken as evidences that these galaxies were undergoing their first bursts of star formation (Sargent & Searle 1970). In fact, one of the most important aspects about BCDs is that they constitute an important

link to the high redshift universe and the early epoch of galaxy formation (Bergvall & Östlin 2002). During the last decade, however, deep imaging of BCDs showed that in addition to bright young stars from the present starburst most of them have an underlying older stellar population (Paderos et al. 1996; Aloisi et al. 1999; Östlin 2000).

One of the challenges of the BCDs is to reconcile their low-observed metallicity with the relatively high star formation rate (SFR) in these galaxies. Matteucci & Chiosi (1983) proposed three possible mechanisms to explain this fact: 1) variations in the initial mass function (IMF); 2) accretion of metal-poor gas; and 3) galactic winds powered by supernovae explosions. According to numerical models, it seems that the last mechanism is the most simple to reproduce the

\* E-mail: rgb@iaa.es

observed properties (see Tolstoy et al. 2009 and references therein for a detailed explanation).

The star formation history (SFH) and the metal content of BCDs must be figured out in order to shed some light on these questions. In the case of SFH, although some advances have been done by means of the fitting of the optical spectrum with stellar populations synthesis (Pérez-Montero et al. 2010), one of the most reliable method consists of the analysis of colour-magnitude diagrams (CMDs). However, this is limited to the closest objects whose stellar population can be resolved. Another important contribution comes from the study of the ionic chemical abundances of elements with a different nucleosynthetic origin, such as oxygen and nitrogen (Mollá et al. 2006). These chemical abundances can be derived very accurately in the metal-poor gas phase of BCDs, where the cooling rate is not efficient, increasing the electron temperature of the ionised gas and enhancing the emissivity of the collisional lines necessary to derive the ionic abundances following the method based on the determination of the electron temperature (Pérez-Montero & Díaz 2003; Hägele et al. 2006).

NGC 6789 is, according to Drozdovsky et al. (2001), the closest BCD to our Galaxy, with a distance modulus of  $(m - M) = 27.80$ , or a distance of 3.6 Mpc. This value yields a linear scale of 17.5 pc arcsec<sup>-1</sup>. Drozdovsky & Tikhonov (2000) imaged NGC 6789 from the ground. They found that it belongs to the iE subtype (following Loose & Thuan 1986 classification), exhibiting the morphology most characteristic of the vast majority of BCDs. NGC 6789 presents several H $\alpha$  emission knots which show evidence of actual star formation activity. It also shows a high surface brightness in its central region and a small radial velocity ( $V_0 = -141$  km s<sup>-1</sup>, Karachentsev & Makarov 1998). NGC 6789’s closeness, spatial isolation and morphology offer the prospect of studying the structure, SFH, and metallicity of different star forming knots within the same BCD.

To investigate these issues, we obtained simultaneous blue and red long-slit observations with the ISIS double-arm spectrograph at the 4.2m William Herschel Telescope (WHT), of the brightest five knots of NGC 6789. We also used archival data from HST/WFPC2, GALEX and H $\alpha$  narrow filter, and B and R broad filters. These images were used to derive the SFH and to give an observational input to derive the properties of the ionising populations with the aid of photoionisation models. These were also used to provide more accurate chemical abundances in each one of the five studied knots of this galaxy and to better understand their differential chemical evolution.

In the following section the long-slit WHT observations and reduction are described and the results from the analysis are presented. In section 3 the optical and UV photometry are described together with the resolved stellar photometry. Finally, we discuss all these results in Section 4 and conclusions are presented in Section 5.

## 2 LONG-SLIT SPECTROSCOPY

### 2.1 Observations and reduction

The long-slit spectrophotometric observations of NGC 6789 were obtained using the ISIS double-beam spectrograph

mounted on the 4.2 m William Herschel Telescope (WHT) of the Isaac Newton group (ING) at the Roque de los Muchachos Observatory on the Spanish island of La Palma. They were acquired on 2005 July 8 during one single night observing run and under photometric conditions, with an average seeing of 0.7 arcsec. The EEV12 and Marconi2 detectors were attached to the blue and red arms of the spectrograph, respectively. The R600B grating was used in the blue covering the wavelength range 3670 - 5070 Å (centred at  $\lambda_c = 4370$  Å), giving a spectral dispersion of 0.45 Å pixel<sup>-1</sup>. On the red arm, the R316R grating was mounted in two different central wavelengths providing a spectral range from 5500 to 7800 Å ( $\lambda_c = 6650$  Å) and from 7600 to 9900 Å ( $\lambda_c = 8750$  Å) with a spectral dispersion of 0.86 Å pixel<sup>-1</sup>. To reduce the readout noise of our images, the observations were taken with the “SLOW” CCD speed. The pixel size for this set-up is 0.2 arcsec for both spectral ranges. The slit width was 1 arcsec, which, combined with the spectral dispersions, yields spectral resolutions of about 1.0 and 3.5 Å FWHM in the blue and red arms, respectively. The instrumental configuration and other details on the exposures are given in the journal of observations in Table 1.

Several bias and sky flat field frames were taken at the beginning and at the end of the night in both arms. In addition, two lamp flat fields and one calibration lamp exposure were taken for each telescope position. The calibration lamp used was +CuAr.

The images were processed and analysed with IRAF<sup>1</sup> routines in the usual manner. The procedure included cosmic rays removal, bias subtraction, division by a normalised flat field and wavelength calibration. Typical wavelength fits to second to third order polynomials were performed using around 40 lines in the blue and 20-25 lines in the red. These fits were done at 100 different locations along the slit in both arms (beam size of 10 pixels) obtaining rms residuals between  $\sim 0.1$  and  $\sim 0.2$  pix. In the last step, the spectra were corrected for atmospheric extinction and flux calibrated. For both arms, BD+254655 standard star observations were used, allowing a good spectrophotometric calibration with an estimated accuracy of about 5%.

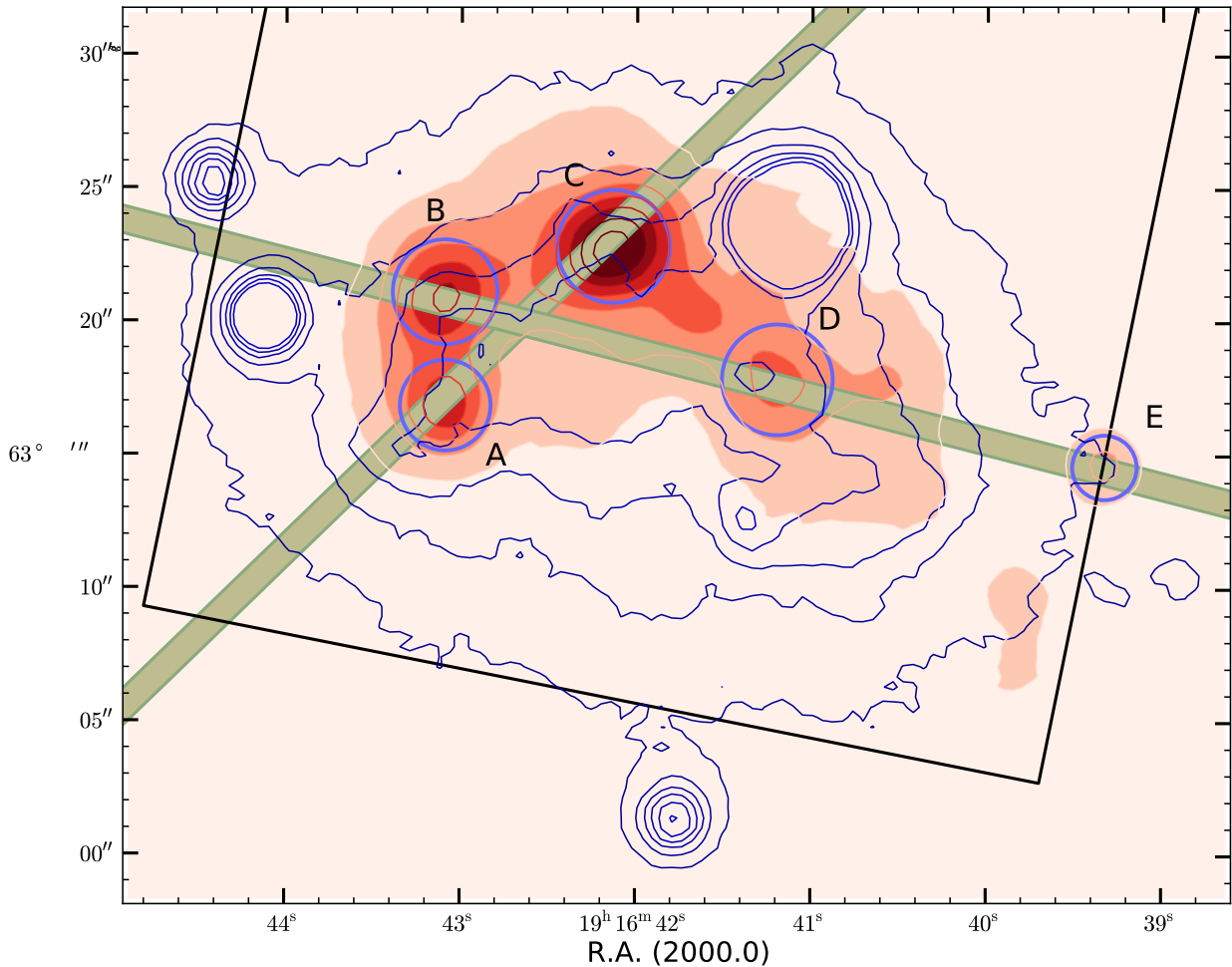
Unfortunately, the sky subtraction in the spectral range from 7600 to 9900 Å left strong residuals from night-sky emission lines and telluric absorption, leaving this part of the spectra unusable and therefore, we were not able to measure with enough accuracy the [SiII]  $\lambda\lambda$  9069,9532 Å lines in any of the five knots.

Figure 1 shows the H $\alpha$  image and continuum contours in the R-band from Gil de Paz et al. (2003) in order to illustrate the position of the slits in relation to the position of the bursts of star formation and the host galaxy. We also show elliptical regions in H $\alpha$  taken to measure the total H $\alpha$  and GALEX flux of the knots (see Section 3.1 below). The five knots are labelled with the first alphabet letters. Knots A and C were taken at PA = 138°, which in average is close to the parallactic angle. In the case of knots B,

<sup>1</sup> IRAF: the Image Reduction and Analysis Facility is distributed by the National Optical Astronomy Observatories, which is operated by the Association of Universities for Research in Astronomy, Inc. (AURA) under cooperative agreement with the National Science Foundation (NSF).

**Table 1.** WHT instrumental configuration

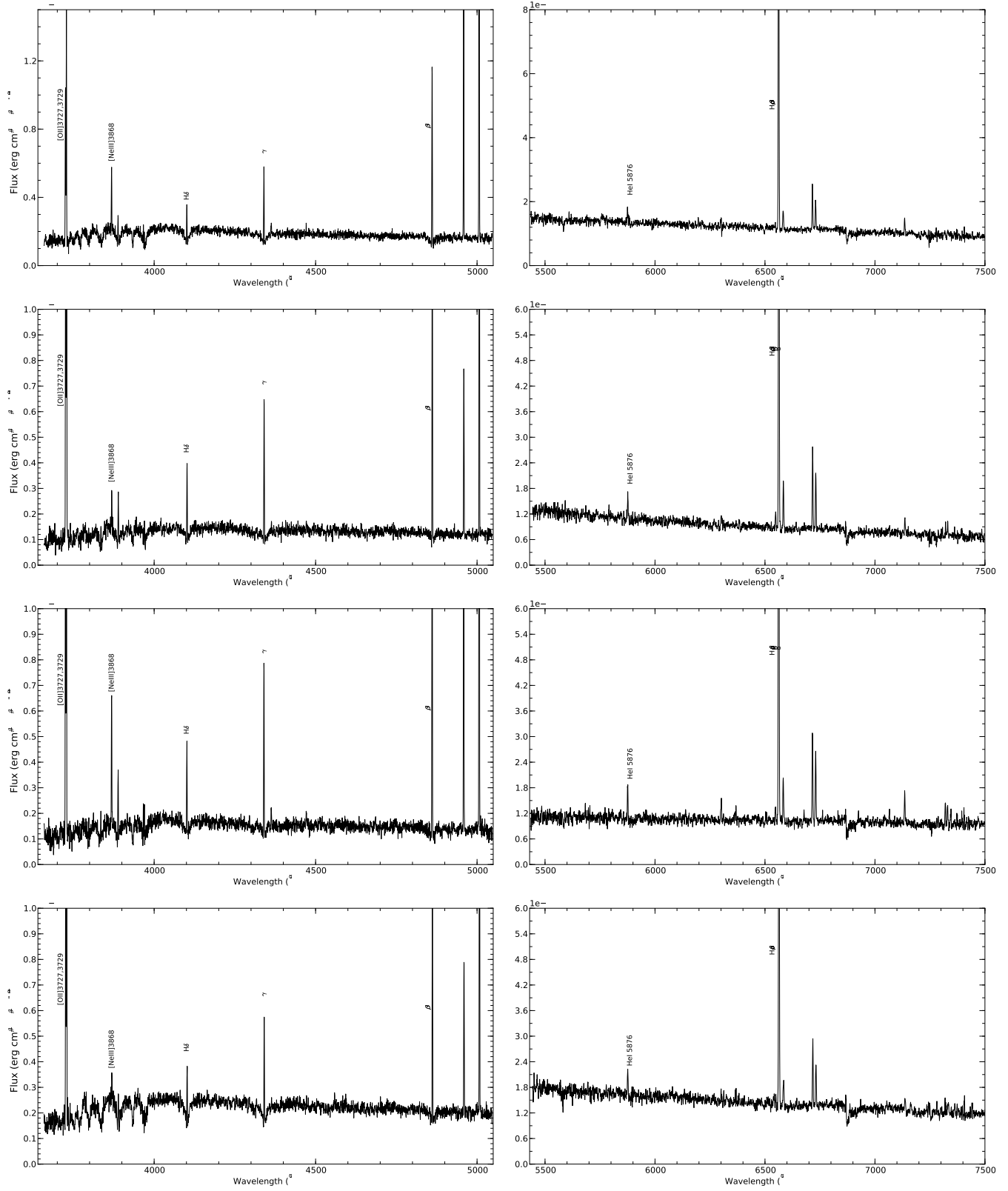
Slit position	Spectral range (Å)	Disp. (Å px <sup>-1</sup> )	FWHM (Å)	Spatial res. ('' px <sup>-1</sup> )	Exposure Time s
S1	3670-5070	0.45	1.0	0.2	4 × 900
S1	5500-7800	0.86	3.5	0.2	2 × 900, 1 × 300
S1	7600-9900	0.86	3.5	0.2	2 × 900
S2	3670-5070	0.45	1.0	0.2	5 × 900
S2	5500-7800	0.86	3.5	0.2	2 × 900, 1 × 300
S2	7600-9900	0.86	3.5	0.2	2 × 900



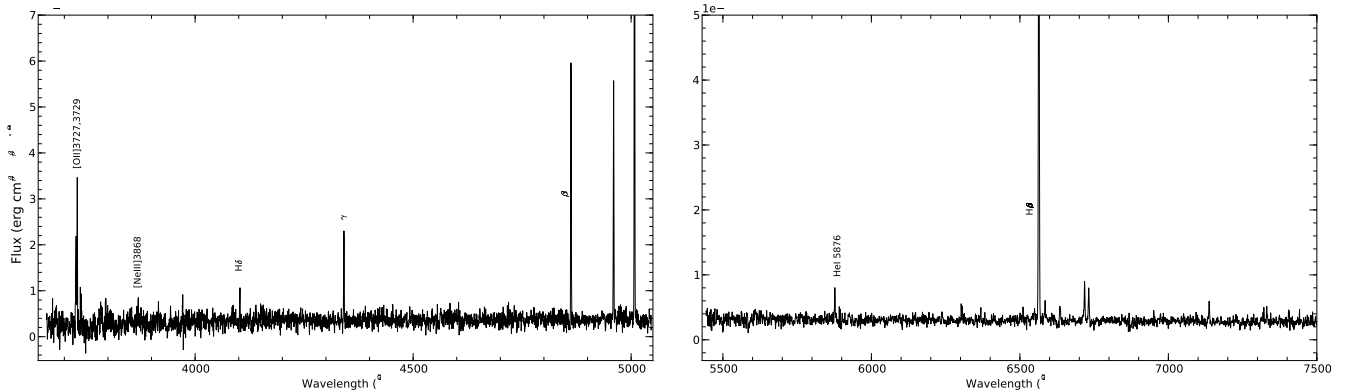
**Figure 1.** H $\alpha$  image of NGC 6789 from Gil de Paz et al. (2003) with the identification of the observed knots (labelled from A to E). We show the regions for which the H $\alpha$  flux was measured and the position of the two slits for the observations described in the text. The R-band contours show the position of the host galaxy. Finally, we also plot part of the rectangle encompassing the field-of-view of the PC chip of the WFPC2 data used to obtain the resolved stellar photometry described in Section 3.2. North is up and east is towards the left-hand side.

D, and E the slit was at PA = 76°, which is in average  $\approx 40^\circ$  off the parallactic angle. Therefore, the observations in this second position can be affected by a certain differential atmospheric refraction (DAR). Nevertheless, taking into account the curves given by Filippenko (1982) for the mean air mass during the observations ( $\approx 1.30$ ), we calculated that the angular deviation between [OII] and [SII] is not larger than the slit width at this P.A. Besides, we checked that the emission line-ratios in the spatial position where both slit positions intersect do not vary in more than the quoted

errors. Nevertheless, the line measurements errors of the second slit position (B, D and E knots) might be larger due to this effect. For the sake of comparison, we also plot in Figure 1 part of the rectangle encompassing the field-of-view (FOV) of the PC chip of the WFPC2 data used to obtain the resolved stellar photometry (see Section 3.2)



**Figure 2.** Blue and red spectra for the knots A, B, C, D, and E of NGC 6789.

Figure 2. – *continued*

## 2.2 Line intensities and reddening correction

The optical calibrated spectra of the five observed knots with some relevant identified emission lines are shown in Figure 2. The spectrum of each knot is split into two panels.

Underlying stellar population in star forming galaxies have several effects in the measure of the emission lines produced by the ionised gas. Balmer and Paschen emission lines are depressed by the presence of absorption wings of stellar origin and does not allow the measure of their fluxes with acceptable accuracy (Diaz 1988). All the properties derived from ratios that involve these lines, like reddening or ionic abundances, will be affected.

We subtracted from the observed spectra the spectral energy distribution of the underlying stellar population found by the spectral synthesis code STARLIGHT<sup>2</sup> (Cid Fernandes et al. 2004, 2005; Mateus et al. 2006). STARLIGHT fits an observed continuum spectral energy distribution using a combination of the synthesis spectra of different single stellar populations (SSPs; also known as instantaneous burst) using a  $\chi^2$  minimisation procedure. We chose for our analysis the SSP spectra from Bruzual & Charlot (2003), based on the STELIB library of Le Borgne et al. (2003), Padova 1994 evolutionary tracks, and a Chabrier (2003) IMF between 0.1 and 100  $M_{\odot}$ . The metallicity of the libraries was strictly constrained following the results derived from Section 4.1. Thus, we fixed the metallicity of the stellar populations to  $Z = 0.004$  ( $\approx 3/10 Z_{\odot}$ ) for the interval  $\log(\text{age}) = [8.1, 8.5]$  and  $Z = 0.001$  ( $\approx 1/12 Z_{\odot}$ ) for  $\log(\text{age}) = \{6.0, 6.4, 6.6, 6.8, 7.0, 7.1, 7.2, 7.9, 8.0, 8.1, 8.2, 8.3, 9.1, 9.2, 9.3, 9.7, 9.8, 9.9, 10.0, 10.1\}$  shown in the SFH solution (see Figure 5). As explained in section 4.1, although both metallicities appear in the youngest burst ( $< 12$  Myr) SFH solution, we assigned the lower metallicity to this event according to the abundances derived in section 2.4. The STARLIGHT code solves simultaneously the ages and relative contributions of the different SSPs and the average reddening. The reddening law from Cardelli et al. (1989) with  $R_V = 3.1$  was used. Prior to the fitting procedure, the spectra were shifted to the rest frame and re-sampled to a

wavelength interval of 1 Å in the entire wavelength range by interpolation, as required by the program. Bad pixels and emission lines were excluded from the final fits.

It should be noted that while emission lines can be masked out, this is not possible for the nebular continuum emission. We tested the contribution of this emission using Starburst99 libraries (SB99; Leitherer et al. 1999) in the same STARLIGHT models and we checked that the nebular continuum does not affect significantly neither the subtraction of the underlying continuum nor the determination of the stellar mass, consistently with the weak gas emission in this galaxy.

The H I series (emitted as a consequence of recombination) were used to determine the extinction, comparing the observed line ratios with the expected theoretical values. Case B (optically thick in all the Lyman lines) is the best simple approximation to describe the physical conditions in the ionisation of the gas. This method takes advantage of the fact that the ratio between the emissivities of two hydrogen recombination lines, which depends on electron temperature and density, is almost constant. As an example, the ratio between the emissivity of  $H\alpha$  and  $H\beta$  is 2.86 for the case B with  $n_e = 100 \text{ cm}^{-3}$  and  $T_e = 10000 \text{ K}$ , and this value varies less than 10% in the range of interest of temperatures and densities for an H II region. We used an iterative method to estimate them, taking as starting values those derived from the measured  $[\text{SII}] \lambda\lambda 6717, 6731 \text{ Å}$  and  $[\text{OIII}] \lambda\lambda 4363, 4959, 5007 \text{ Å}$ . A least square fit of the measured decrements to the theoretical ones, computed based on the data by Storey & Hummer (1995), was performed that provides the reddening coefficient,  $c(H\beta)$ , and adopting the extinction law given by Cardelli et al. (1989) with  $R_V = 3.1$ . Due to the large error introduced by the presence of the underlying population, only the strongest Balmer emission lines ( $H\alpha$ ,  $H\beta$ ,  $H\gamma$ , and  $H\delta$ ) were used.

Line fluxes for the most relevant emission lines were measured using the `splot` task in IRAF. Balmer lines were obtained from the STARLIGHT residual spectra, while the rest of the lines were measured on the original spectra. We checked in all spectra that the Starlight models properly reproduce the observed Balmer absorption profiles<sup>4</sup>. The

<sup>2</sup> The STARLIGHT project is supported by the Brazilian agencies CNPq, CAPES and FAPESP and by the France-Brazil CAPES/Cofecub program.

<sup>3</sup>  $Z_{\odot} = 0.0122$

<sup>4</sup> From several fitting experiments using other libraries it is found



statistical errors associated with the observed emission line fluxes were calculated using the expression:

$$\sigma_l = \sigma_c \sqrt{N \left( 1 + \frac{EW}{N\Delta} \right)} \quad (1)$$

where  $\sigma_l$  is the error in the observed line flux,  $\sigma_c$  represents the standard deviation in a box near the measured emission line and stands for the error in the continuum placement,  $N$  is the number of pixels used in the measure of the line flux,  $EW$  is the line equivalent width, and  $\Delta$  is the wavelength dispersion in Å per pixel (Gonzalez-Delgado et al. 1994). This expression takes into account the error in the continuum and the photon count statistics of the emission line.

Table 2 gives the equivalent widths and the emission-line fluxes relative to 1000-F(H $\beta$ ), before and after reddening correction, in the optical spectra of the five observed knots, together with the reddening constants and their errors, their corresponding A(V) value<sup>5</sup> and the extinction-corrected H $\beta$  flux. We also provide the adopted reddening curve,  $f(\lambda)$  normalised to H $\beta$ . The errors in the emission-line ratios were obtained by propagating in quadrature the observational errors in the emission-line fluxes and the reddening constant uncertainties.

### 2.3 Electron densities and temperatures

The electron density and temperatures of the ionised gas were derived from the emission line data using the same procedures as in Pérez-Montero & Díaz (2003), based on the five-level statistical equilibrium atom approximation in the IRAF task `temden` (De Robertis et al. 1987; Shaw & Dufour 1995). See Hägele et al. (2008) and Appendix B of García-Benito (2009) for a description of the temperature and densities relations, respectively. We took as sources of error the uncertainties associated with the reddening-corrected emission-line fluxes and we propagated them through our calculations.

Electron densities were derived from the [SII]  $\lambda\lambda$  6717,6731 Å and [OII]  $\lambda\lambda$  3726,3729 Å line ratios, which are representative of the low-excitation zone of the ionised gas. In all cases they provide upper limits, which are remarkably similar for both ions. In the case of the oxygen lines, the spectral dispersion does not allow the total resolution of the lines, and they were deblended by a multi-Gaussian fit. The upper limits for the electron density are lower in all cases than the critical value for collisional de-excitation.

We computed three electron temperatures, T([OII]), T([OIII]) and T([SIII]), for each of the five knots. The auroral [OIII] 4363 was detected in all the five knots with sufficient signal-to-noise, and the [OIII] electron temperature was derived directly from the ratio (I(4959 Å) + I(5007 Å))/I(4363 Å).

The auroral [OII] 7319 and [OII] 7330 lines from the 2F

multiplet are emission-line doublets. Due to the spectral resolution, we report here the sum of each doublet. Using the calculated [OIII] electron temperatures, we checked that the contribution by direct recombination is negligible for these lines (Liu et al. 2000). For knot A and D, the intensity of the [OII]  $\lambda\lambda$  7319,7330 Å did not allow an accurate measure, therefore we derived their [OII] temperature from T([OIII]) using the relation based on the photoionisation models described in Pérez-Montero & Díaz (2003), which takes into account explicitly the dependence of T([OII]) on the electron density.

Although we could measure the [SIII]  $\lambda$  6312 Å in some of the knots, we were not able to get the [SIII]  $\lambda$  9069,9532 Å lines, so we estimated the [SIII] temperature from the empirical relation

$$t([SIII]) = (1.19 \pm 0.08)t([OIII]) - (0.32 \pm 0.10) \quad (2)$$

found by Hägele et al. (2006).

The electron densities and temperatures derived in the five knots of NGC 6789 are listed in Table 3 along with their corresponding errors.

### 2.4 Ionic abundances

We derived the ionic abundances of the different chemical species using the brightest available emission lines detected in the optical spectra using the task `ionic` of the STSDAS package in IRAF (see Hägele et al. 2008). The total abundances were derived by taking into account, when required, the unseen ionisation stages of each element, resorting to the ionisation correction factors (ICFs) for each species derived from the photoionisation models described in Section 4.2 below.

$$\frac{X}{H} = ICF(X^i) \frac{X^{+i}}{H^+} \quad (3)$$

#### 2.4.1 Helium abundance

Four of the strongest helium emission lines, HeI  $\lambda\lambda$  4471, 5876, 6678, and 7065 Å were used to calculate He<sup>+</sup>/H<sup>+</sup>. The last two lines were only detected with enough signal-to-noise in knot C. Also in this knot, HeII  $\lambda$  4686 was measured, allowing the calculation of twice ionised He.

Helium lines arise mainly from pure recombination; however, they could have some contribution from collisional excitation as well as being affected by self-absorption and, if present, by underlying stellar absorptions (see Olive & Skillman 2001, for a complete treatment), but we checked that these absorptions produce negligible variations in the measure of the lines in the STARLIGHT subtracted spectra.

We took the electron temperature of [OIII] as representative of the zone where the He emission arises and we used the equations given by Olive & Skillman (2001) to derive the He<sup>+</sup>/H<sup>+</sup>, using the theoretical emissivities scaled to H $\beta$  from Smits (1996) and the expressions for the collisional correction factors from Kingdon & Ferland (1995). To calculate the helium twice ionised, we used the equation found by Kunth & Sargent (1983). We did not take into account, however, the corrections for fluorescence since the involved

that the resolution of the SSP spectra is a critical factor for Starlight in order to fit the absorption lines.

<sup>5</sup>  $c(H\beta) = 0.4656 \cdot A(V)$ , using Cardelli et al. (1989) and  $R_V = 3.1$ .

**Table 2.** Observed and reddening corrected relative line intensities [ $F(H\beta)=I(H\beta)=1000$ ] with their corresponding errors for the five knots. The adopted reddening curve,  $f(\lambda)$  (normalised to  $H\beta$ ), the equivalent width of the emission lines, the extinction-corrected  $H\beta$  intensity, the reddening constant  $c(H\beta)$  and the corresponding  $A(V)$  are also given.

NGC 6789-A					NGC 6789-B		
$\lambda$ (Å)	$f(\lambda)$	$F(\lambda)$	$EW(\text{Å})$	$I(\lambda)$	$F(\lambda)$	$EW(\text{Å})$	$I(\lambda)$
3726 [OII]	0.322	$896 \pm 19$	-15.0	$979 \pm 63$	$1186 \pm 17$	-34.9	$1277 \pm 80$
3729 [OII]	0.322	$1241 \pm 16$	-20.7	$1357 \pm 84$	$1744 \pm 16$	-51.9	$1878 \pm 116$
3835 H9	0.299	$37 \pm 10$	-0.6	$40 \pm 11$	$80 \pm 4$	-3.5	$85 \pm 7$
3868 [NeIII]	0.291	$302 \pm 17$	-2.8	$327 \pm 26$	$153 \pm 14$	-3.7	$164 \pm 17$
3889 HeI+H8	0.286	$153 \pm 6$	-2.6	$166 \pm 12$	$146 \pm 10$	-4.5	$156 \pm 14$
3968 [NeIII]+H7	0.266	$81 \pm 8$	-1.3	$88 \pm 10$	...	...	...
4102 H $\delta$	0.229	$247 \pm 5$	-3.9	$263 \pm 16$	$248 \pm 16$	-6.7	$261 \pm 22$
4340 H $\gamma$	0.157	$454 \pm 11$	-7.2	$474 \pm 28$	$448 \pm 7$	-12.4	$465 \pm 26$
4363 [OIII]	0.149	$63 \pm 3$	-0.7	$66 \pm 5$	$23 \pm 4$	-0.4	$23 \pm 4$
4471 HeI	0.115	$36 \pm 4$	-0.4	$37 \pm 5$	$37 \pm 6$	-0.7	$39 \pm 7$
4861 H $\beta$	0.000	$1000 \pm 10$	-17.3	$1000 \pm 47$	$1000 \pm 12$	-29.1	$1000 \pm 48$
4959 [OIII]	-0.026	$1240 \pm 12$	-16.0	$1231 \pm 57$	$512 \pm 12$	-11.4	$509 \pm 26$
5007 [OIII]	-0.038	$3801 \pm 13$	-50.1	$3762 \pm 167$	$1492 \pm 9$	-33.0	$1479 \pm 66$
5876 HeI	-0.203	$102 \pm 14$	-1.6	$97 \pm 14$	$96 \pm 16$	-2.3	$92 \pm 16$
6312 [SIII]	-0.264	$11 \pm 2$	-0.2	$10 \pm 2$	$16 \pm 5$	-0.5	$16 \pm 5$
6548 [NII]	-0.296	$28 \pm 5$	-0.5	$26 \pm 5$	$61 \pm 9$	-1.8	$57 \pm 8$
6563 H $\alpha$	-0.298	$3038 \pm 29$	-57.0	$2797 \pm 38$	$3003 \pm 15$	-89.3	$2807 \pm 20$
6584 [NII]	-0.300	$136 \pm 10$	-2.5	$126 \pm 9$	$186 \pm 11$	-5.6	$174 \pm 10$
6717 [SII]	-0.318	$277 \pm 10$	-5.0	$254 \pm 10$	$314 \pm 9$	-9.5	$292 \pm 8$
6731 [SII]	-0.320	$188 \pm 10$	-3.4	$172 \pm 9$	$217 \pm 10$	-6.6	$202 \pm 9$
7136 [ArIII]	-0.374	$112 \pm 7$	-2.4	$101 \pm 7$	$76 \pm 7$	-2.7	$70 \pm 7$
7319 [OII]	-0.398	...	...	...	$46 \pm 6$	-1.6	$42 \pm 6$
7330 [OII]	-0.400	...	...	...	$35 \pm 4$	-1.2	$32 \pm 4$
$I(H\beta)(\text{erg seg}^{-1} \text{cm}^{-2})$			2.70e-15			3.19e-15	
$c(H\beta)$			$0.12 \pm 0.02$			$0.10 \pm 0.02$	
$A(V)$			$0.26 \pm 0.04$			$0.21 \pm 0.04$	
NGC 6789-C					NGC 6789-D		
$\lambda$ (Å)	$f(\lambda)$	$F(\lambda)$	$EW(\text{Å})$	$I(\lambda)$	$F(\lambda)$	$EW(\text{Å})$	$I(\lambda)$
3726 [OII]	0.322	$940 \pm 13$	-29.1	$1020 \pm 64$	$1159 \pm 26$	-15.4	$1267 \pm 82$
3729 [OII]	0.322	$1377 \pm 12$	-42.4	$1494 \pm 92$	$1712 \pm 21$	-22.5	$1871 \pm 116$
3835 H9	0.299	$47 \pm 9$	-1.4	$50 \pm 10$	...	...	...
3868 [NeIII]	0.291	$300 \pm 12$	-5.2	$323 \pm 23$	$105 \pm 9$	-0.9	$114 \pm 12$
3889 HeI+H8	0.286	$169 \pm 12$	-5.5	$182 \pm 17$	$167 \pm 20$	-2.4	$180 \pm 24$
3968 [NeIII]+H7	0.266	$74 \pm 9$	-2.3	$79 \pm 11$	...	...	...
4102 H $\delta$	0.229	$246 \pm 16$	-5.9	$261 \pm 22$	$244 \pm 7$	-3.2	$260 \pm 16$
4340 H $\gamma$	0.157	$446 \pm 7$	-12.4	$464 \pm 26$	$444 \pm 10$	-5.3	$464 \pm 27$
4363 [OIII]	0.149	$59 \pm 3$	-1.3	$61 \pm 5$	$24 \pm 8$	-0.2	$25 \pm 8$
4471 HeI	0.115	$37 \pm 5$	-0.7	$38 \pm 6$	$36 \pm 6$	-0.3	$37 \pm 7$
4686 HeII	0.050	$26 \pm 5$	-0.5	$26 \pm 5$	...	...	...
4861 H $\beta$	0.000	$1000 \pm 8$	-27.1	$1000 \pm 47$	$1000 \pm 10$	-12.1	$1000 \pm 47$
4959 [OIII]	-0.026	$1170 \pm 9$	-26.9	$1163 \pm 53$	$607 \pm 11$	-6.2	$602 \pm 29$
5007 [OIII]	-0.038	$3471 \pm 11$	-75.0	$3438 \pm 153$	$1750 \pm 12$	-16.7	$1732 \pm 78$
5876 HeI	-0.203	$96 \pm 14$	-2.8	$91 \pm 14$	$104 \pm 20$	-1.3	$98 \pm 19$
6312 [SIII]	-0.264	$19 \pm 2$	-0.6	$18 \pm 2$	$22 \pm 6$	-0.3	$20 \pm 5$
6548 [NII]	-0.296	$51 \pm 11$	-1.6	$47 \pm 10$	$51 \pm 12$	-0.8	$48 \pm 11$
6563 H $\alpha$	-0.298	$3000 \pm 23$	-92.8	$2797 \pm 30$	$3026 \pm 16$	-46.7	$2814 \pm 21$
6584 [NII]	-0.300	$145 \pm 11$	-4.5	$135 \pm 10$	$149 \pm 6$	-2.2	$138 \pm 6$
6678 HeI	-0.313	$27 \pm 5$	-0.8	$25 \pm 4$	...	...	...
6717 [SII]	-0.318	$307 \pm 7$	-9.4	$285 \pm 7$	$300 \pm 17$	-4.4	$277 \pm 16$
6731 [SII]	-0.320	$236 \pm 8$	-7.2	$219 \pm 8$	$206 \pm 14$	-3.0	$191 \pm 13$
7065 HeI	-0.364	$23 \pm 5$	-0.7	$21 \pm 4$	...	...	...
7136 [ArIII]	-0.374	$87 \pm 11$	-2.7	$80 \pm 10$	$80 \pm 16$	-1.3	$73 \pm 15$
7319 [OII]	-0.398	$44 \pm 4$	-1.4	$40 \pm 4$	...	...	...
7330 [OII]	-0.400	$42 \pm 3$	-1.3	$38 \pm 2$	...	...	...
$I(H\beta)(\text{erg s}^{-1} \text{cm}^{-2})$			3.93e-15			2.61e-15	
$c(H\beta)$			$0.11 \pm 0.02$			$0.12 \pm 0.02$	
$A(V)$			$0.24 \pm 0.04$			$0.26 \pm 0.04$	

**Table 2.** – *Continued*

$\lambda$ (Å)	$f(\lambda)$	NGC 6789-E		
		$F(\lambda)$	$EW(\text{Å})$	$I(\lambda)$
3726 [OII]	0.322	$347 \pm 51$	-30.5	$492 \pm 94$
3729 [OII]	0.322	$398 \pm 25$	-28.3	$563 \pm 77$
3868 [NeIII]	0.291	$62 \pm 11$	-2.2	$86 \pm 18$
4102 H $\delta$	0.229	$145 \pm 10$	-7.6	$186 \pm 25$
4340 H $\gamma$	0.157	$374 \pm 9$	-11.9	$443 \pm 48$
4363 [OIII]	0.149	$20 \pm 9$	-0.6	$23 \pm 11$
4471 HeI	0.115	$36 \pm 5$	-1.7	$41 \pm 7$
4861 H $\beta$	0.000	$1000 \pm 13$	-35.7	$1000 \pm 93$
4959 [OIII]	-0.026	$842 \pm 15$	-22.9	$818 \pm 75$
5007 [OIII]	-0.038	$2358 \pm 17$	-60.0	$2263 \pm 201$
5876 HeI	-0.203	$124 \pm 23$	-4.3	$100 \pm 20$
6548 [NII]	-0.296	$42 \pm 14$	-1.3	$39 \pm 13$
6563 H $\alpha$	-0.298	$3090 \pm 32$	-98.9	$2836 \pm 42$
6584 [NII]	-0.300	$69 \pm 12$	-2.1	$64 \pm 11$
6717 [SII]	-0.318	$225 \pm 23$	-8.4	$202 \pm 21$
6731 [SII]	-0.320	$207 \pm 18$	-8.4	$186 \pm 17$
7136 [ArIII]	-0.374	$80 \pm 8$	-2.8	$68 \pm 6$
7319 [OII]	-0.398	$27 \pm 4$	-1.2	$22 \pm 3$
7330 [OII]	-0.400	$20 \pm 8$	-1.0	$17 \pm 6$
$I(H\beta)(\text{erg s}^{-1} \text{cm}^{-2})$		2.94e-15		
$c(H\beta)$		$0.47 \pm 0.06$		
$A(V)$		$1.00 \pm 0.10$		

**Table 3.** Electron densities and temperatures for the five knots. Densities units are in  $\text{cm}^{-3}$  and temperatures in  $10^4$  K.

	NGC 6789-A	NGC 6789-B	NGC 6789-C	NGC 6789-D	NGC 6789-E
$n([\text{SII}])$	80:	60:	60:	90:	300:
$n([\text{OII}])$	60:	70:	60:	70:	250:
$t([\text{OIII}])$	$1.44 \pm 0.05$	$1.36 \pm 0.10$	$1.44 \pm 0.05$	$1.30 \pm 0.15$	$1.16 \pm 0.18$
$t([\text{OII}])$	$1.35 \pm 0.06^a$	$1.18 \pm 0.10$	$1.41 \pm 0.08$	$1.21 \pm 0.10^a$	$1.33 \pm 0.25$
$t([\text{SIII}])^b$	$1.38 \pm 0.16$	$1.30 \pm 0.19$	$1.38 \pm 0.16$	$1.22 \pm 0.24$	$1.06 \pm 0.25$

<sup>a</sup> From a relation with  $T([\text{OIII}])$  based on photoionisation models<sup>b</sup> From an empirical relation with  $T([\text{OIII}])$ 

helium lines have negligible dependence on optical-depth effects and the observed knots have low densities.

The results obtained for each line and their corresponding errors are presented in Table 4. For knot C, the total abundance of He was calculated by adding directly the two ionic abundances,  $\text{He}/\text{H} = (\text{He}^+ + \text{He}^{2+})/\text{H}^+$ . Also given in the table is the adopted value for  $\text{He}^+/\text{H}^+$ , a weighted average of the values, using the error of each line as weight.

#### 2.4.2 Ionic abundances from forbidden lines

The oxygen ionic abundance ratios,  $\text{O}^+/\text{H}^+$  and  $\text{O}^{2+}/\text{H}^+$ , were derived from the [OII]  $\lambda\lambda 3726, 3729$  Å and [OIII]  $\lambda\lambda 4959, 5007$  Å lines, respectively using the appropriate electron temperature for each ion.

The ionic abundance of nitrogen,  $\text{N}^+/\text{H}^+$ , was derived from the intensities of the [NII]  $\lambda\lambda 6548, 6584$  Å lines assuming that  $T([\text{NII}]) \approx T([\text{OII}])$ .

For sulphur, we derived  $\text{S}^+/\text{H}^+$  abundances from the fluxes of the [SII] emission lines at  $\lambda\lambda 6717, 6731$  Å assuming that  $T([\text{SII}]) \approx T([\text{OII}])$ . Since we were not able to measure the near infrared [SIII]  $\lambda\lambda 9069, 9532$  Å we derived the  $\text{S}^{2+}/\text{H}^+$  abundances using  $T([\text{SIII}])$  and [SIII]  $\lambda 6312$  Å by means of the equation

$$12 + \log(\text{S}^{2+}/\text{H}^+) = \frac{\log \frac{I(6312)}{I(H\beta)}}{I(H\beta)} + 6.74 + \frac{1.672}{t} - 0.595 \log t \quad (4)$$

Neon ionic abundance was estimated from the [Ne III] emission line at  $\lambda 3869$  Å. For this ion, we took the electron temperature of [OIII] as representative of the high excitation zone (Peimbert & Costero 1969).

[Ar III]  $\lambda 7136$  Å was the only argon line detected in the spectra and the abundance of  $\text{Ar}^{2+}$  was calculated assuming that  $T([\text{ArIII}]) \approx T([\text{SIII}])$  (Garnett 1992).

The ionic abundances -and their corresponding errors- for each observed element for the five knots are given in Table 5.

### 3 OPTICAL AND UV PHOTOMETRY

#### 3.1 H $\alpha$ and GALEX photometry

We analysed the H $\alpha$  image of the galaxy, retrieved from the Palomar/Las Campanas atlas of blue compact dwarf galaxies (Gil de Paz et al. 2003). We defined elliptical apertures on this image for each of the five knots extracted in the spectroscopic observations and we measured all the flux inside



**Table 4.** Ionic chemical abundances for helium.

	NGC 6789-A	NGC 6789-B	NGC 6789-C	NGC 6789-D	NGC 6789-E
He <sup>+</sup> /H <sup>+</sup> (4471)	0.077 ± 0.011	0.080 ± 0.015	0.079 ± 0.013	0.076 ± 0.014	0.082 ± 0.015
He <sup>+</sup> /H <sup>+</sup> (5876)	0.075 ± 0.011	0.071 ± 0.013	0.072 ± 0.012	0.076 ± 0.015	0.073 ± 0.016
He <sup>+</sup> /H <sup>+</sup> (6678)	...	...	0.071 ± 0.013	...	...
He <sup>+</sup> /H <sup>+</sup> (7065)	...	...	0.074 ± 0.016	...	...
He <sup>+</sup> /H <sup>+</sup>	0.076 ± 0.010	0.075 ± 0.012	0.074 ± 0.009	0.076 ± 0.011	0.077 ± 0.011
He <sup>2+</sup> /H <sup>+</sup> (4686)	...	...	0.0023 ± 0.0006	...	...
He/H	...	...	0.076 ± 0.009	...	...

**Table 5.** Ionic chemical abundances derived from forbidden emission lines, ICFs<sup>a</sup> and total chemical abundances for elements heavier than helium.

	NGC 6789-A	NGC 6789-B	NGC 6789-C	NGC 6789-D	NGC 6789-E
12 + log(O <sup>+</sup> /H <sup>+</sup> )	7.43 ± 0.04	7.82 ± 0.11	7.42 ± 0.07	7.73 ± 0.11	7.16 ± 0.23
12 + log(O <sup>2+</sup> /H <sup>+</sup> )	7.63 ± 0.04	7.28 ± 0.07	7.59 ± 0.04	7.41 ± 0.13	7.68 ± 0.17
<b>12 + log(O/H)</b>	7.84 ± 0.04	7.93 ± 0.10	7.81 ± 0.05	7.90 ± 0.12	7.80 ± 0.18
12 + log(N <sup>+</sup> /H <sup>+</sup> )	6.03 ± 0.04	6.37 ± 0.07	6.08 ± 0.06	6.22 ± 0.07	5.85 ± 0.16
ICF(N <sup>+</sup> )	3.57	1.57	4.57	1.97	4.09
<b>12 + log(N/H)</b>	6.58 ± 0.04	6.57 ± 0.07	6.74 ± 0.06	6.51 ± 0.07	6.50 ± 0.16
log(N/O)	-1.26 ± 0.06	-1.37 ± 0.12	-1.07 ± 0.08	-1.38 ± 0.14	-1.30 ± 0.24
12 + log(S <sup>+</sup> /H <sup>+</sup> )	5.70 ± 0.03	5.91 ± 0.07	5.75 ± 0.05	5.83 ± 0.07	5.70 ± 0.14
12 + log(S <sup>2+</sup> /H <sup>+</sup> )	5.88 ± 0.16	6.14 ± 0.23	6.09 ± 0.16	6.35 ± 0.30	...
ICF(S <sup>+</sup> + S <sup>2+</sup> )	1.11	1.01	1.24	1.01	7.64 <sup>b</sup>
<b>12 + log(S/H)</b>	6.20 ± 0.11	6.35 ± 0.18	6.41 ± 0.11	6.48 ± 0.25	6.58 ± 0.14
log(S/O)	-1.64 ± 0.12	-1.58 ± 0.20	-1.41 ± 0.12	-1.41 ± 0.27	-1.22 ± -0.25
12 + log(Ne <sup>2+</sup> /H <sup>+</sup> )	7.00 ± 0.06	6.77 ± 0.10	7.00 ± 0.06	6.68 ± 0.17	6.75 ± 0.20
ICF(Ne <sup>2+</sup> )	1.39	1.61	1.28	2.07	1.22
<b>12 + log(Ne/H)</b>	7.14 ± 0.06	6.98 ± 0.10	7.11 ± 0.06	7.00 ± 0.17	6.82 ± 0.20
log(Ne/O)	-0.70 ± 0.07	-0.95 ± 0.14	-0.70 ± 0.08	-0.90 ± 0.21	-0.96 ± 0.27
12 + log(Ar <sup>2+</sup> /H <sup>+</sup> )	5.67 ± 0.08	5.56 ± 0.12	5.56 ± 0.09	5.63 ± 0.17	5.70 ± 0.19
ICF(Ar <sup>2+</sup> )	1.12	1.21	1.15	1.14	1.10
<b>12 + log(Ar/H)</b>	5.72 ± 0.08	5.64 ± 0.12	5.62 ± 0.09	5.68 ± 0.17	5.74 ± 0.19
log(Ar/O)	-2.12 ± 0.09	-2.28 ± 0.16	-2.19 ± 0.10	-2.22 ± 0.21	-2.06 ± 0.22

<sup>a</sup> ICFs estimated from tailored photoionisation models (see Section 4.2)<sup>b</sup> ICF(S<sup>+</sup>)

the elliptical apertures up to the isophote corresponding to the 50% of the peak of the intensity for each knot (see Figure 1). The total fluxes and the corresponding luminosities at the adopted distance are listed in Table 6 with their corresponding errors. The observed H $\alpha$  fluxes were corrected in each knot for dust extinction using the values of  $c(\text{H}\beta)$ , given in Table 2. We also list in the same table the size of each knot, as the radius of the circular aperture whose area is equal to that encompassed by the elliptical aperture. As can be seen in Figure 1, NGC 6789 has an H $\alpha$  major axis of 740 pc and 560 pc for its minor axis, measured using an elliptical aperture that encompasses the isophote at  $3\sigma$  over the level of the sky background noise. The total flux inside this isophote (not extinction-corrected) is  $(2.0 \pm 0.1) \times 10^{-12} \text{ erg s}^{-1} \text{ cm}^{-2}$ .

The *Galaxy Evolution Explorer* (GALEX; Martin et al. 2005; Morrissey et al. 2005) far-ultraviolet (FUV;  $\lambda_{\text{ref}} = 1530 \text{ \AA}$ ,  $\Delta\lambda = 400 \text{ \AA}$ ) and near-ultraviolet (NUV;  $\lambda_{\text{ref}} = 2310 \text{ \AA}$ ,  $\Delta\lambda = 1000 \text{ \AA}$ ) images of NGC 6789 were retrieved from the Nearby Galaxies Survey (NGS). We used the same elliptical apertures defined in the H $\alpha$  image to obtain the FUV and NUV fluxes in each knot. In Table 6 we show for each knot both the FUV and NUV magnitudes once extinction corrected together with the colour index FUV-NUV, all of them in AB mags. As typical sizes of the studied star-

forming knots are lower than the GALEX point-spread function (PSF), some aperture effects to the measured UV fluxes that cannot be quantified may exist. However, the characterization of the knots by the corresponding colour indices are less affected by this effect than the total flux measurements in these regions, as we checked by taking different aperture sizes around the position of the knots.

As can be seen, the four brightest knots (from A to D) have similar UV luminosities both in FUV and NUV, being the knot D the brightest one, although this is not the brightest knot in H $\alpha$ . Regarding colours, knots B and C present redder UV colours as compared with the other three knots.

### 3.2 WFPC2 Photometry

*Hubble Space Telescope* (HST) Wide Field Planetary Camera 2 (WFPC2) images of NGC 6789 were retrieved from the HST archive. We discuss photometry based on the images taken in 2000 July-September (GO-8122) through two continuum filters: F555W (V) and F814W (I). Each camera images onto a Loral 800×800 CCD which gives a plate scale of  $0''.046 \text{ pixel}^{-1}$  for the PC camera and  $0''.10 \text{ pixel}^{-1}$  for the three WF cameras, with a readout noise of  $\sim 5 \text{ e}^-$  and a gain of  $7 \text{ e}^-/\text{DN}$  for this observations. The central star-forming

**Table 6.** Properties of the individual knots as measured in the  $H\alpha$  and GALEX photometry.

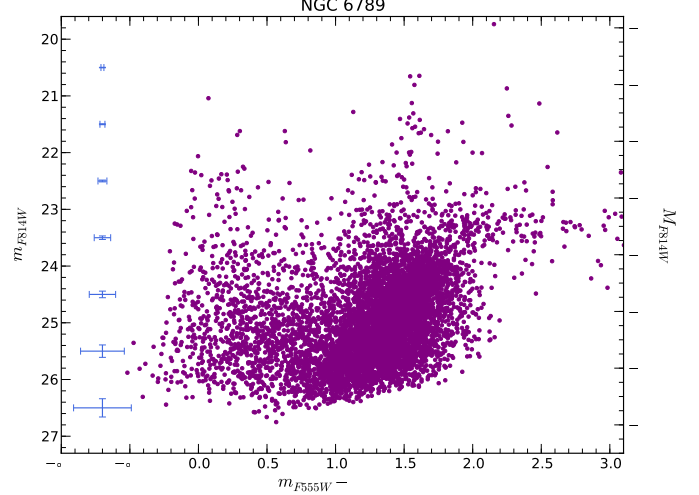
	NGC 6789-A	NGC 6789-B	NGC 6789-C	NGC 6789-D	NGC 6789-E
$\log F(H\alpha)$ (erg/s/cm <sup>2</sup> )	$-13.96 \pm 0.03$	$-13.85 \pm 0.03$	$-13.69 \pm 0.03$	$-14.03 \pm 0.03$	$-14.17 \pm 0.03$
$\log L(H\alpha)$ (erg/s)	$37.23 \pm 0.02$	$37.34 \pm 0.02$	$37.50 \pm 0.03$	$37.17 \pm 0.02$	$37.02 \pm 0.01$
Radius (pc)	30	34	37	36	21
FUV (mag)	$20.00 \pm 0.14$	$20.00 \pm 0.16$	$20.18 \pm 0.20$	$19.71 \pm 0.15$	$21.24 \pm 0.04$
NUV (mag)	$19.86 \pm 0.08$	$19.69 \pm 0.09$	$19.86 \pm 0.10$	$19.68 \pm 0.09$	$21.18 \pm 0.01$
FUV - NUV (mag)	$0.14 \pm 0.16$	$0.28 \pm 0.19$	$0.31 \pm 0.22$	$0.03 \pm 0.18$	$0.06 \pm 0.04$

region of NGC 6789 was centered in the PC camera in all images using three different pointings. The scale of the PC CCD at NGC 6789, for which we assumed a distance modulus of  $(m - M) = 27.80$  (Drozdovsky et al. 2001), is  $0.80 \text{ pc pixel}^{-1}$ . Table 7 lists the details concerning the WFPC2 data. Figure 3 shows the HST WFPC2 images of NGC 6789 in F555W and F814W filters. The contours are drawn from FUV and NUV GALEX images, respectively. The aperture of knot E defined in the  $H\alpha$  image and the rectangle encompassing the FOV of the PC chip of the WFPC2 data are also shown for reference.

The stellar photometric analysis was performed with the HSTphot package (Dolphin 2000b). This package is specifically designed for use with HST WFPC2 images and uses a library of Tiny Tim (Krist 1995) undersampled PSFs for different locations of the star on the camera and of the star within the pixel, to centre the star and to find its magnitude, given in the flight system magnitude. The first step was to run the **mask** task using the HST data quality file (**c1f**) to mask out the bad pixels and other image defects. The next step was to run **crmask** for cosmic ray removal. We used a registration factor of 0.5 and  $\sigma$ -threshold of 3. It has the capability of cleaning images that are not perfectly aligned, and it can handle images from different filters. After cosmic-ray rejection, sets of images of each filter at a common pointing were combined into a single image, using the routine **coadd**. Since there are two images per pointing, we ended up with 3 images per filter. The sky computation is made by **getsky**, which takes all pixels in an annulus around each pixel, determines the sky value and calculates the sky background map. These sky values are used only as a starting guess in the HSTphot photometry. The final step requires the use of the **hotpixels** procedure on each combined image, which uses the result from **getsky** and tries to locate and remove all hot pixels. This is an important step, since hot pixels can create false detections and also, can throw off the PSF solutions.

The main **hstphot** routine was run on the images in the F555W and F814W bands. This task performs stellar PSF photometry on multiple images from different filters and pointings (providing the dithering pattern, it analyses the dithering image as a whole), including alignment and aperture corrections, as well as PSF modifications to correct for errors of geometric distortion via the Holtzman et al. (1995) distortion correction equations and the 34th row error, noted by Shaklan et al. (1995) (see also Anderson & King 1999), and correction for charge transfer inefficiency (Dolphin 2000a). We enabled the determination of a “local sky” value (option 2).

We selected “good stars” from the **hstphot** output. Object types were classified as good star, possible unresolved binary, bad star, single-pixel cosmic ray or hot pixel, and ex-

**Figure 4.** CMD of NGC 6789 with average photometric uncertainties per magnitude bin.

tended object. To ensure selecting high fidelity point sources, we also used the “sharpness” parameter (absolute value to be  $\leq 0.35$ ), a measure of the quality of the fit ( $\chi^2 \leq 2.5$ ) and a minimum signal-to-noise ratio of 10 to reject false star detections in regions with structured nebulosity or artifacts. The final number of stars detected in the PC chip with these parameters in both filters were 7410.

To quantify the completeness and systematic uncertainty of the photometry, a grid of artificial stars was generated on a 2-dimensional CMD and distributed according to the flux of the images with an artificial star routine provided by HSTphot. The parameters of the routine are the minimum and maximum of the measured colour and magnitude. The magnitude steps used were multiple of 0.5, while colour steps are by 0.25. The artificial stars were distributed on the CMD in accordance with the number observed. Approximately 60,000 fake stars were added in each image (at different trials, in order to leave the crowding conditions unaltered) and were given random magnitudes and colours in the observed range. The 50% completeness of the F555W filter is reached at 26.9 magnitude, while for the F814W filter is 25.6 mag.

The final CMD of NGC 6789 with typical photometric errors per magnitude bin is shown in Figure 4.

**Table 7.** Journal of HST/WFPC2 observations of NGC 6789. The images were obtained in 2000 July–September for the cycle 8 program GO-8122, with Regina Schulte-Ladbeck as PI. The object of study is centered in the PC chip.

Filter	RA (J2000)	Dec (J2000)	Exposure (s)	Observation ID
F555W	19:16:37.77	+63:58:37.2	$2 \times 1300$	U5BF0301R, U5BF0302R
	19:16:37.73	+63:58:37.4	$2 \times 1400$	U5BF0303R, U5BF0304R
	19:16:37.68	+63:58:37.6	$2 \times 1400$	U5BF0305R, U5BF0306R
F814W	19:16:37.77	+63:58:37.2	$2 \times 1300$	U5BF0401R, U5BF0402R
	19:16:37.73	+63:58:37.4	$2 \times 1400$	U5BF0403R, U5BF0404R
	19:16:37.68	+63:58:37.6	$2 \times 1400$	U5BF0405R, U5BF0406R

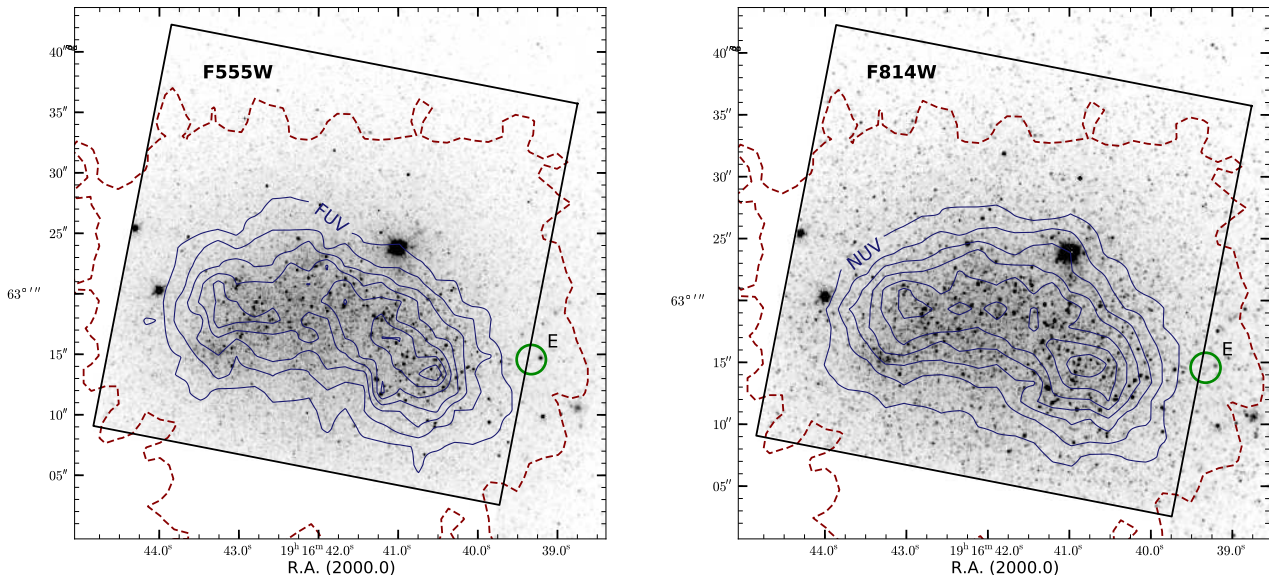


**Figure 3.** HST WFPC2 images of NGC 6789 in continuum filters F555W and F814W. The solid contours are drawn from FUV and NUV GALEX images, respectively. The dashed contour corresponds to the isophote at  $3\sigma$  over the level of the sky background of the Palomar/Las Campanas  $H\alpha$  image. The aperture of knot E defined in the  $H\alpha$  image and the rectangle encompassing the FOV of the PC chip of the WFPC2 data are also shown for reference. North is up and east is towards the left-hand side.

## 4 DISCUSSION

### 4.1 Star formation history and stellar populations

Studies to obtain information on the star formation of composite stellar systems have been proven to be very successful (see e.g., Aparicio et al. 1997; Hernandez et al. 2000; Dolphin 2002). Any SFH recovery method relies on the assumption that a composite stellar population can be considered simply as the combination of SSPs, assigning a certain relative weight to each SSP. The observed CMD is compared with theoretical ones created via Monte-Carlo methods for a variety of IMFs, binary fractions, star-formation laws, etc., extracting the stellar information from isochrones or stellar evolution tracks. Observed and theoretical CMDs are divided into boxes and converted into two-dimensional histograms of stellar density as function of colour and magnitude (Hess diagrams) and compared using statistical methods.

For the analysis of this work, we used the StarFISH code<sup>6</sup> developed by Harris & Zaritsky (2001). This code was

successfully used in a number of cases (e.g. Harris & Zaritsky 2004; Brown et al. 2006; Williams et al. 2007; Harris & Zaritsky 2009; García-Benito et al. 2011). Using determinations of the interstellar extinction, photometric errors, and distance moduli, it uses minimisation of a chi-squared-like statistics technique to find the linear combination of single-component stellar population models that best fit an observed CMD. The ages and metallicities of the underlying stellar population are characterized by the ages and metallicities of the CMDs included in the best, while SFR at each age is provided by the weights given to the CMDs.

The theoretical isochrones chosen for analysis were those of Marigo et al. (2008)<sup>7</sup> for ages in the range 1 Myr–14 Gyr. This data set includes models with age bins spaced logarithmically since the CMD changes much more rapidly at young ages than at old ones. We chose the two metallicity values closest to the observed ones (see Section 2.4), namely  $Z = \{0.001, 0.004\}$ . Marigo et al. (2008) provide metallicities in the range  $0.0001 \leq Z \leq 0.03$ . Nevertheless, for the sake of consistency we selected only the same values that were available for the STARLIGHT libraries (Bruzual & Charlot 2003). The photometric error and completeness

<sup>6</sup> Available at <http://www.noao.edu/staff/jharris/SFH/>

<sup>7</sup> Available at <http://stev.oapd.inaf.it/cgi-bin/cmd/>

estimates were taken directly from the results of the artificial star experiments described in Section 3.2. We adopted a Salpeter IMF with a spectral index of -1.35 from 0.1-100  $M_{\odot}$  Salpeter (1955). This assumption is likely to be valid since our CMD does not contain stars with masses  $< 1 M_{\odot}$ . The binary fraction was set to a value of 0.5.

Our reference value for NGC 6789 distance modulus is  $(m - M) = 27.80 \pm 0.13 \pm 0.18$ , value reported by Drozdovsky et al. (2001) using the tip of the red giant branch distance method. The Galactic extinction is  $A_V = 0.212$ , value provided by Schlegel et al. (1998) extinction maps for an area with radius equal to 5 arcmin around NGC 6789, remarkably close to the reddening value obtained from our spectroscopic data (Section 2.2). Nevertheless, we built a set of models to explore the space of parameters. The SFH recovery is repeated for each point in the grid  $(m - M)$  vs  $A_V$ , and then we built a final  $\chi^2_{min}$  map for the solutions. We explored the space of parameters in steps of 0.01 in distance modulus and extinction. To evaluate the errors of the recovered solutions, we generated a series of synthetic CMDs using the best-fitting SFR and find a correspondence between the  $\chi^2_{min}$  and the confidence level of significance.

Although it is tempting to perform a SFH analysis for each knot, the resulting individual CMDs, taken to be as the stars included inside the defined ellipses (see Figure 1 and subsection 3.1), do not contain enough stars<sup>8</sup> and, therefore, the large errors associated with each individual SFH prevent us to draw any conclusion. At any rate, the distribution of stars in each individual CMD is very similar for all the knots. Thus, we use the entire CMD of the galaxy to derive the global SFH.

Figure 5 shows the overall best-fitting StarFISH solution for the SFH of NGC 6789, located at  $(m - M) = 27.83 \pm 0.06$  and  $A_V = 0.64 \pm 0.08$ , where the errors stand for the  $1\sigma$  confidence level. The errors in the star formation diagram only allow the consideration of a few main bursts in the SFH. Regarding the lower metallicity ( $Z = 0.001$ ), the solution shows a few bursty events around 1.6 Gyr and 6-10 Gyr, followed by a more recent burst around 100 Myr and a very young one during the last 12 Myr. As for the higher metallicity ( $Z = 0.004$ ), only one event between 150-300 Myr is clearly seen. Although for the very young stars ( $< 12$  Myr) both metallicities present a significant error, we take  $Z = 0.001$  as the metallicity for the youngest event, as derived from the nebular analysis (see section 2.4). The SFR, according to StarFISH's results, was stronger around 100 Myr, with a peak of  $0.015 M_{\odot}/\text{yr}$ .

In the light of these results, we used the age-metallicity solution derived from the CMD as a prior to constrain the libraries of the STARLIGHT code, used to fit the spectra of the five knots (see Section 2.2 for more details). In left panel of Figure 6 we show the age distribution of the light fraction obtained from STARLIGHT for each knot under the constraints mentioned above. Another fitting was carried out without any specific age-metallicity constrain in order to compare it with the results of the first fitting. These are shown in the right panel of Figure 6. As can be seen, all knots present a very young stellar population, with ages younger than 10 Myr, responsible for the ionisation of the gas, com-

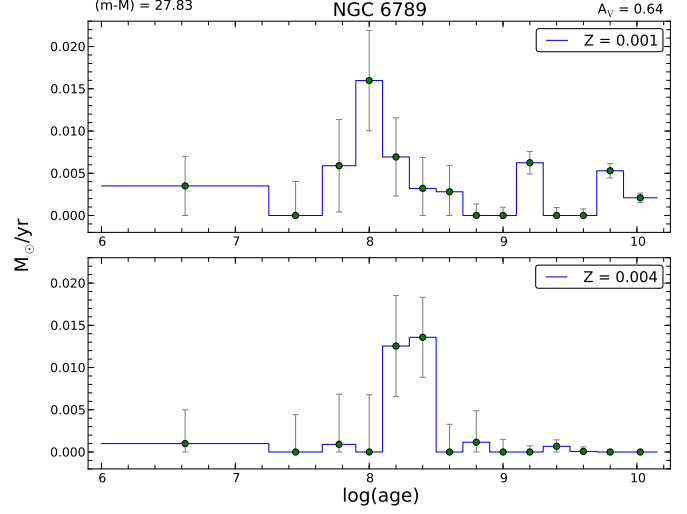


**Figure 5.** Best StarFISH SFH fit derived from the HST optical observations of the resolved stellar populations for NGC 6789. The best distance modulus and extinction values are also shown.

bined with other older populations. The presence of these old populations is confirmed with the detection of absorption metal lines of Ca II K  $\lambda$  3933 Å and Ca II H  $\lambda$  3968 Å characteristic of old stellar populations, except for knot E, in which these features are marginally detected. The combination of these two different stellar population is also obtained by Pérez-Montero et al. (2010) in a sample of 10 BCDs using the same technique. In terms of mass, more than the 80% comes from the older population. The estimated total stellar mass and the fraction of the mass of the stellar population with an age younger than 10 Myr with respect to the total mass are given in Table 8. The stellar masses were corrected for aperture effects, with factors calculated using the ratio between the extinction-corrected H $\alpha$  fluxes measured in the elliptical regions of the photometry and those measured in the extracted long-slit observations for each knot. In the same table we show the EW(H $\beta$ ) values calculated once the contribution of the older stellar populations was removed, in order to use EW(H $\beta$ ) to derive the properties of the ionising stellar population (see Section 4.2). The inner extinctions calculated by STARLIGHT for each fit are also listed in the same table. Finally, the results for the non-constrained case are given in the second row for each knot. The values from Table 8 show that those fits obtained from non-constrained libraries do not significantly alter some of the properties of the stellar populations, such as the total stellar mass and the correction factor for EW(H $\beta$ ), even that some relevant differences appear in the age and metallicity distribution of the resulting SFHs. Therefore, we relied on the general chemical evolution solution derived by StarFISH to constrain the age-metallicity libraries of STARLIGHT. At any rate, the general distribution of the light is similar in both cases. We recall that the CMD SFH (StarFISH) is derived for the whole galaxy, while the spectra SFH (STARLIGHT) is derived for each individual knot.

Less significant is the difference of the fitted spectra between both cases. For these two particular metallicities, the variation of the intensity of the first four Balmer lines on the residual spectra for each knot is well within the observa-

<sup>8</sup> Specially Knot E, part of which falls outside the PC FOV.



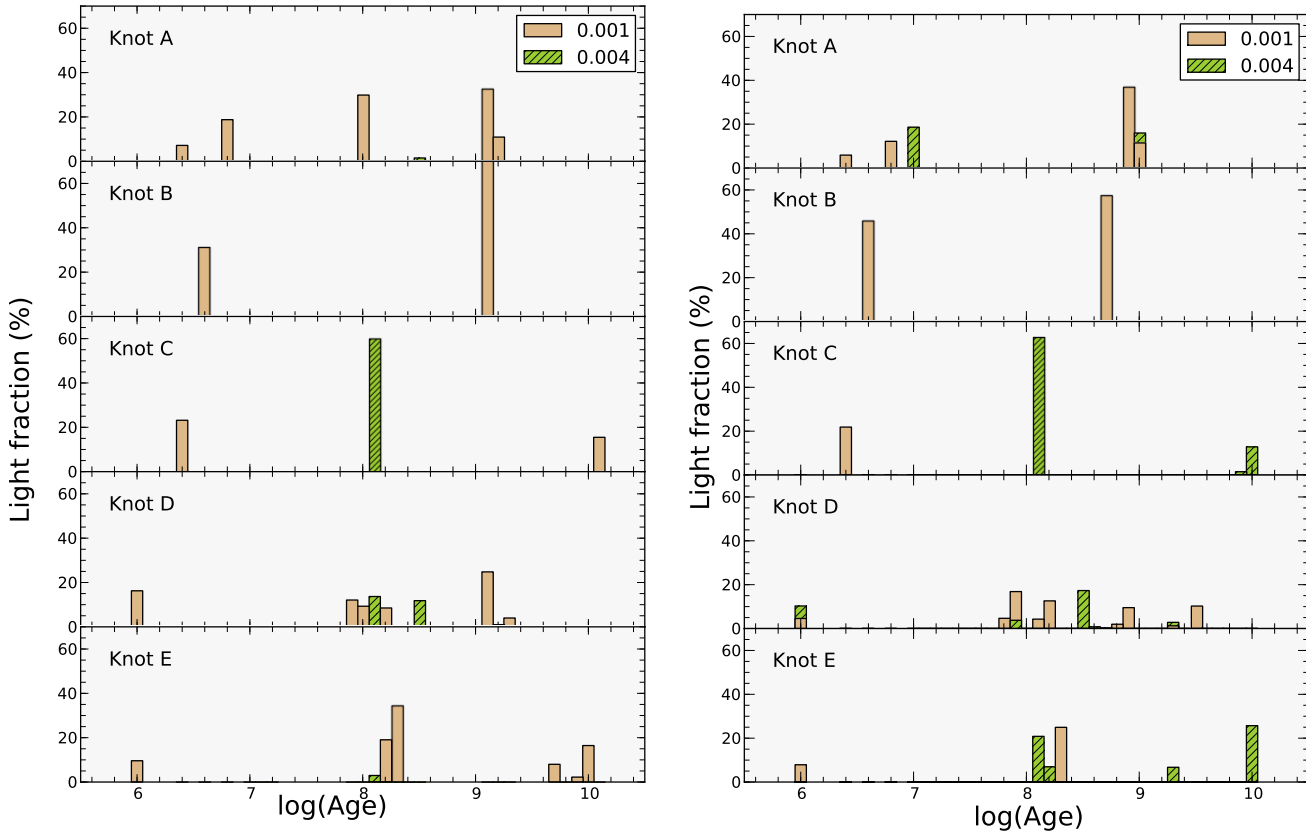


**Figure 6.** Histograms of the distribution (light fraction) of the best fit derived by STARLIGHT for the spectra of the five knots of NGC 6789. The left panel corresponds to the fits using the constraints obtained by the CMD analysis, while the right panel shows the fits using non-constrained age-metallicity libraries.

tional errors when using one or the other case. The change of age-metallicity distribution in the libraries only affects significantly in these two particular cases to the SFH in the assignments of the metallicity of the stellar populations, but the overall derived age distribution is very similar.

Regarding the extinction, we find some discrepancies between the values found by STARLIGHT and those derived using Balmer decrements. However, the average extinction value for all knots ( $0.52 \pm 0.16$ ) is very close to the CMD best fitting value given by StarFish ( $0.64 \pm 0.08$ ). It should be noted, though, that in principle it is not expected to find the same values in the gas and the stellar population.

#### 4.2 Ionising stellar populations and photoionisation models

Among the properties of the young ionising populations that can be derived from optical spectroscopy are their stellar masses and ages. The former can be derived from the  $H\alpha$  luminosity and  $EW(H\beta)$  (e.g. Díaz 1998).  $H\alpha$  luminosity can also be used to estimate the SFR and the mass of ionised hydrogen. The age can be estimated by using the  $EW(H\beta)$  as compared to sequences of evolutionary synthesis models. In our case, the contamination of the older underlying population to the  $H\beta$  continuum was removed by using the analysis made with STARLIGHT. As can be seen in Table 8, these corrections are quite different between the knots, going from a 3% in the case of knot B to a 42% in the case of knot E.

**Table 8.** Properties of the stellar populations as obtained with STARLIGHT for each knot of NGC 6789, including the inner extinction, the aperture corrected total stellar mass, the mass of stars younger than 10 Myr ( $M_{ion*}$ ), and the  $EW(H\beta)$  corrected for the contribution of the older population. The first row for each knot corresponds to the constrained age-metallicity libraries, while the second row is for the unconstrained case.

ID	A(V) (mag)	log $M_*$	log $M_{ion*}$	$EW(H\beta)_c$ (Å)
Knot A	0.4	5.34	3.69	23
	0.4	5.35	3.81	19
Knot B	0.3	5.26	3.16	30
	0.7	5.22	3.68	30
Knot C	0.7	6.00	4.03	49
	0.6	5.97	3.95	51
Knot D	0.5	5.42	3.79	24
	0.5	5.51	3.66	24
Knot E	0.7	5.16	2.71	84
	0.5	5.21	2.47	95

Nevertheless, as already shown by Pérez-Montero & Díaz (2007) and later in Pérez-Montero et al. (2010) for other samples of BCDs, the corrected  $EW(H\beta)$  are still much lower than the expected values for the ionisation of stellar clusters younger than 10 Myr. The  $H\text{I}$  mass can be estimated using the CO observations of this object reported by Leroy et al. (2005) (marginally detected and thus, an upper limit) and using the  $X_{CO}$  factor at the appropriate metallicity pro-



**Table 9.** Properties of the individual knots derived from tailored photoionisation models compared with the observed values.

	NGC 6789-A		NGC 6789-B		NGC 6789-C		NGC 6789-D		NGC 6789-E	
	Mod.	Obs.	Mod.	Obs.	Mod.	Obs.	Mod.	Obs.	Mod.	Obs.
log L(H $\alpha$ ) (erg/s)	37.32	37.23 $\pm$ 0.02	37.34	37.34 $\pm$ 0.02	37.51	37.50 $\pm$ 0.03	37.18	37.17 $\pm$ 0.02	37.03	37.02 $\pm$ 0.01
Radius (pc)	7	30	33	34	22	37	10	36	5	21
FUV-NUV (mag)	0.17	0.14 $\pm$ 0.16	0.28	0.28 $\pm$ 0.19	0.30	0.31 $\pm$ 0.22	0.22	0.03 $\pm$ 0.18	0.10	0.06 $\pm$ 0.04
I([OII]/I(H $\beta$ ))	2.30	2.34 $\pm$ 0.15	3.33	3.16 $\pm$ 0.20	2.35	2.51 $\pm$ 0.16	3.05	3.14 $\pm$ 0.20	1.09	1.06 $\pm$ 0.04
I([OIII]/I(H $\beta$ ))	3.82	3.76 $\pm$ 0.17	1.47	1.48 $\pm$ 0.07	3.45	3.44 $\pm$ 0.15	1.72	1.73 $\pm$ 0.08	2.30	2.26 $\pm$ 0.20
12+log(O/H)	7.93	7.84 $\pm$ 0.04	7.82	7.93 $\pm$ 0.10	7.79	7.81 $\pm$ 0.05	7.77	7.90 $\pm$ 0.12	7.64	7.80 $\pm$ 0.18
-EW(H $\beta$ ) (Å)	21	23	30	30	48	49	29	24	80	84
Age (Myr)	5.4	...	4.2	...	3.5	...	5.2	...	3.9	...
Dust-to-gas ratio	0.026	...	0.34	...	0.12	...	0.15	...	0.015	...
Abs. factor ( $f_d$ )	5.34	...	7.28	...	8.21	...	4.37	...	2.23	...

posed by Magrini et al. (2011) to derive the H I column density. For the adopted distance of NGC 6789 this gives a total mass of  $\log(M_{HI}/M_\odot) \sim 6$ . Thus, this implies that dust absorption could be the main responsible of the disagreement between expected and observed EW(H $\beta$ ). Thus, both L(H $\alpha$ ) and EW(H $\beta$ ) must be corrected using the dust absorption factor ( $f_d$ ) before the derivation of the properties of the ionising cluster. This correction must be done even after the extinction correction, because it corresponds to the fraction of ionising photons absorbed by the dust and, therefore, not absorbed and re-emitted by the gas:

$$Q(H) = f_d \times Q_{obs}(H) \quad (5)$$

To estimate both  $f_d$  and the ages of the ionising cluster for each knot, we made tailored photoionisation models using the code CLOUDY v.08.00 (Ferland et al. 1998). Our models assume a one-dimensional structure, with the central ionising cluster and a gas and dust geometry, and compute the emergent spectrum. For each knot we took as input the Starburst99 libraries (Leitherer et al. 1999; Vázquez & Leitherer 2005), based on stellar model atmospheres from Smith et al. (2002), Geneva evolutionary tracks with high stellar mass loss (Meynet et al. 1994), a Kroupa IMF (Kroupa 2002) in two intervals (0.1-0.5 and 0.5-100  $M_\odot$ ) with different exponents (1.3 and 2.3 respectively), the theoretical wind model (Leitherer et al. 1992) and a supernova cut-off of 8  $M_\odot$ . We fixed the metallicity of the stellar populations to  $Z = 0.001$  ( $\approx 1/12 Z_\odot$ ), which corresponds to the closest total oxygen abundance measured using the direct method in all the knots. We also fixed the density of particles to match the value derived in each knot from the [SII] emission-line ratio and the chemical abundances in the gas (except oxygen) to match those derived using the direct method. Those species that were not measured were put to scale with the solar proportions measured by Asplund et al. (2009). Although not all species are expected to follow solar proportions, the deviation of this assumption does not affect the results of our models of all the other studied species. In each knot, we used an iterative method to find the values of the free parameters (oxygen abundance, dust-to-gas ratio, number of ionising photons, internal radius, filling factor, and age of the ionising cluster) that better fit the observed properties (3727 Å [OII]/H $\beta$ , 5007 Å [OIII]/H $\beta$ , 12+log(O/H), L(H $\alpha$ ), and FUV-NUV colour index). The fitted properties along with the derived cluster age and  $f_d$  in the corresponding model for each knot are shown in Table 9. The FUV-

NUV colours were obtained by convolving the model output emergent spectrum for each knot with the shape of the corresponding GALEX filter, performing a direct measure of the resulting total flux, and finally calculating the corresponding colour in AB magnitudes.

The assumptions taken for the models described above may be an oversimplification as they do not take into account the three-dimensional structure of the ionized gas and the dust. Besides, we cannot take as input parameter the dust-to-gas ratio of this galaxy and possible uncertainties related with the adopted synthesis stellar atmospheres can affect the final result.

As can be seen, the observed properties are generally well fitted by the models, by assuming different geometries and dust-to-gas ratios without noticeably changing the derived metallicity of the gas. According to our results,  $f_d$  correlates better with the FUV-NUV index than with the reddening constant derived from the Balmer decrement in the optical spectra. For instance, knot C has the highest  $f_d$  with the lowest c(H $\beta$ ) and, in contrast, knots A and E have the lowest  $f_d$  and the highest c(H $\beta$ ). This could be indicative of a complex inner dust structure which is not well traced by the reddening constant derived from the Balmer decrement. Regarding the cluster ages, our results indicate that all knots have ionising cluster in a range of ages between 3.5 Myr for knot C and 5.4 Myr for knot A. The youngest cluster appears in knot C, although knot E, which has a very low  $f_d$  correction, has the lowest EW(H $\beta$ ). The age sequence in the studied knots does not correspond to any specific spatial order.

The total masses of the ionising clusters were also derived by using the number of ionising photons and the ages obtained from the respective CLOUDY models and the Starburst99 libraries of the corresponding synthesis cluster atmospheres. These are listed in Table 10. As can be seen, the stellar masses of the bursts in the four first knots are quite similar, while knot E has the lowest value. These masses are in agreement within 0.3 dex with the masses derived for the younger stellar population using the fitting to the optical spectrum made with STARLIGHT (Table 8).

Once the  $f_d$  were estimated for the five knots, it was possible to derive the properties that depend on the corrected total L(H $\alpha$ ), including the mass of ionised hydrogen, the Star Formation Strengths (SFS, defined as the total mass of gas transformed into stars during the burst) and the SFR. These are listed in Table 10, along with the values for the

**Table 10.** Properties of ionising stellar populations in the knots as derived using the  $Q(H^0)$  value obtained from the photoionisation models.

ID	$\log Q(H^0)$ (erg/s)	$\log M_{burst}$ ( $M_\odot$ )	$\log M(HII)$ ( $M_\odot$ )	$\log SFS$ ( $M_\odot$ )	SFR ( $10^{-3} M_\odot/\text{yr}$ )
Knot A	49.94	3.82	3.45	4.34	1.04
Knot B	50.09	3.65	3.60	4.32	1.47
Knot C	50.31	3.69	3.82	4.54	2.44
Knot D	49.69	3.52	3.20	4.09	0.59
Knot E	49.25	2.73	2.76	3.48	0.21
NGC 6789 <sup>a</sup>	51.49	...	5.00	5.89	36.97

<sup>a</sup> Values derived from the  $H\alpha$  image, not corrected for extinction.

whole galaxy. The total ionised masses of the gas clouds in each knot were calculated using Osterbrock (1989):

$$M_{H^+} = Q(H^0) \frac{m_p}{n_e \alpha_B} \quad (6)$$

assuming case B,  $n_e = 100 \text{ cm}^{-3}$ , and  $\alpha_B \sim 2.59 \times 10^{-13} \text{ cm}^{-3} \text{ s}^{-1}$ . The individual knots show masses of ionised hydrogen of the order of hundreds of solar masses for knot E and up to  $\sim 6600 M_\odot$  in knot C. In the case of the whole galaxy, the total flux described in Section 3.1 can be converted into  $(1.0 \pm 0.1) \times 10^5 M_\odot$  of ionised hydrogen, comparable to knot A of the Giant Extragalactic HII Region NGC 5471 in M101 (García-Benito et al. 2011) or to the whole NGC 604 giant HII region in M33 (Relaño & Kennicutt 2009).

It is known that the SFR determined from  $H\alpha$  is sensitive to several uncertainties, as those related with the extinction and the assumed IMF. Besides, not always all the ionising photons are absorbed, being the escape fraction of ionising radiation from individual HII regions (in nearby galaxies) between 15% and 50% (Kennicutt 1998). We applied the calibration by Oti-Floranes & Mas-Hesse (2010)<sup>9</sup>, which makes a distinction between instantaneous (IB) and extended burst (EB). We used our extinction and dust absorption corrected  $H\alpha$  luminosity (except for the value of the whole galaxy) and a Salpeter IMF in the range 0.1-100  $M_\odot$  as input. For the IB case, the value given by the calibration is the SFS. The SFS values in Table 10 were calculated using the age provided by the calibration, namely 4, 5, and 6 Myr, closest to the age estimated from the photoionisation models. According to this calibration, the mass of gas transformed in stars during the actual burst in each knot is of the order of tens of thousands of solar masses, except for knot E, which is one order of magnitude lower.

We provide as well the SFR, for the EB case (continuous star formation), as a reference value. Regarding the SFR of the whole galaxy, the value estimated by means of the  $H\alpha$  flux is slightly higher than the peak obtained from the CMD (see Figure 5). The SFR for BCDs spans from a few  $10^{-3}$  to several times  $10^1 M_\odot/\text{yr}$  (Hopkins et al. 2002; Zhao et al. 2011), showing NGC 6789 not a particularly high value.

Although our models are able to reproduce much of the observational information both in the optical and the UV, some of their limitations must be taken into account. It is

possible that the  $EW(H\beta)$  could be modified owing to great fractions of leaked photons. However, comparing the mass of ionised gas in this galaxy [ $\log(M/M_\odot) \sim 5$ , see Table 10] with the mass of neutral hydrogen does not support this scenario, but taking into account the oversimplified geometry of our models it cannot be ruled out completely. In this sense, as the long-slit does not cover entirely the gas-emission from the knots, the  $EW(H\beta)$  are lower limits. Nonetheless, the aperture factors derived from the direct comparison with the  $H\alpha$  image do not lead to a satisfactory solution.

Larger dust-to-gas ratios and  $f_d$  than typical values for HII regions with larger metallicity (e.g. Inoue 2001) were derived by the models in all knots in order to fit the observed  $EW(H\beta)$  and FUV-NUV colours. However, these values cannot be taken as representative of the whole galaxy but only for the analysed star-forming knots, considering that the fraction of ionised-to-neutral gas is quite small, as mentioned above, and that this galaxy does not present a very high IR luminosity (i.e. it does not appear in the IRAS catalogue). We have run other set of models with standard dust-to-gas ratios, but they do not fit the observables mentioned above. The dust-to-gas ratios could be considerably decreased by assuming different geometries of the gas and dust inside the HII regions, but this approach is beyond the scope of this work.

Finally, our results about the masses and ages of the ionising clusters must be used only as a guiding signpost, as the involved masses range in a regime ( $\sim 10^4 M_\odot$ ) where stochastic fluctuations in the IMF can be important (Cervino & Valls-Gabaud 2003; Cervino & Luridiana 2006). In this sense, IMF sampling effects (Pflamm-Altenburg et al. 2007, 2009) can also alter our results, as there can be a lower number of massive stars than expected for the mass range of these knots.

### 4.3 Densities, temperatures and chemical abundances

The derived densities, both for [SII] and [OII], are very similar for the first four knots, being lower than  $100 \text{ cm}^{-3}$ . Interestingly, knot E, located in the outskirts of the galaxy, shows a density twice higher than the knots located in the central part of the galaxy. At any rate, these densities are typical of low density environments found in BCDs.

Regarding electron temperatures,  $T([OIII])$  was measured in the five knots, with errors which depend on the quality of the spectrum in each knot going from 3% in knot A up to 13% in knot E. The first four star-forming regions

<sup>9</sup> Their web tool can be found at <http://www.laeff.cab.inta-csic.es/research/sfr/>

show very similar [OIII] temperatures, all within a relatively narrow range, between 13000 and 14300 K, while knot E has a lower temperature by about 2000 K. To our knowledge, there is no previous report on  $T([OIII])$  for this galaxy in the literature.

$T([OII])$  was also measured in three of the knots (B, C, and E) and it was estimated in the other two knots by means of relations between these temperatures and the measured value of  $T([OIII])$ . The knot C, which is the brightest in  $H\alpha$ , has in average higher temperatures.

We derived oxygen, nitrogen, sulphur, neon and argon total abundances in all the studied knots by taking the ionic abundances calculated in Section 2.4 and the ICFs estimated in our tailored photoionisation models. As in the case of temperatures, no other direct abundance determination exists in the literature for this galaxy. In average, NGC 6789 shows an oxygen abundance characteristic of the low values found in strong line BCDs, with values in all knots in the range of  $12 + \log(O/H) = 7.80-7.93$ , what is compatible with a similar abundance in all knots taking into account the errors. This behaviour, i.e. showing different star forming knots within a BCD close abundance values (i.e.,  $< 0.2$  dex), is also found in other objects using both long-slit spectroscopy (Papaderos et al. 2006; Cairós et al. 2009; Pérez-Montero et al. 2009; Hägele et al. 2011) and integral field spectroscopy (Kehrig et al. 2008; Pérez-Montero et al. 2011), or in HII complexes in spiral galaxies with a similar spatial scale (Kennicutt et al. 2003; García-Benito et al. 2010).

Since nitrogen and oxygen have different nucleosynthetic origins, their ratio is related to the chemical history of galaxies. Primary nitrogen synthesis is thought to occur in intermediate-mass stars in the CNO process during hydrogen burning being hence independent of the initial heavy-element abundances, while secondary nitrogen production is expected to be produced in stars of all masses (Vila Costas & Edmunds 1993). At low metallicity, most part of nitrogen has a primary origin and a constant  $\log(N/O)$  ratio is observed. However, the  $N/O$  values found in the studied knots of NGC 6789 range in an interval (from -1.38 to -1.26) is sensibly higher than the observed values for other BCDs or low-metallicity dwarf irregular galaxies (Izotov & Thuan 1999; Vílchez & Iglesias-Páramo 2003; van Zee & Haynes 2006; Pérez-Montero & Contini 2009), which is around  $\log(N/O) \approx -1.6$ . In the case of knot C, this ratio is even higher, with a value of -1.07. The cause of these relatively high  $N/O$  can be partially found in the corresponding ICFs derived by the models as the total nitrogen abundances derived from the assumption  $N/O \approx N^+/O^+$  give lower  $N/O$  values in knots A [ $\log(N/O) = -1.41$ ] and C [ $\log(N/O) = -1.34$ ], although still higher within the errors than the typical  $N/O$  value for BCDs.

On the other hand, several causes are cited in the literature to explain this overabundance of nitrogen in low-metallicity environments (e.g. the pollution of the ISM by Wolf-Rayet stellar winds), but it is especially indicative in this case that we found this overabundance in the five knots, which present different evolutionary and excitation properties. Therefore, the high  $N/O$  is apparently related with some other process affecting all the ISM of the galaxy. The fall of pristine gas in the galaxy could explain the  $N/O$  overabundance (Köppen & Hensler 2005) and, at same time, the

triggering of the star formation in different places of the galaxy with very short time intervals between them.

The ratio of the alpha elements, sulphur, neon, and argon, to oxygen should be constant and show no dependence on the oxygen abundance, since all are products of  $\alpha$ -processes in the same massive stars that make oxygen. The derived  $\log(S/O)$  ratios range between -1.64 and -1.41 in the four first knots and it is sensibly higher in knot E, but in this knot the derivation is much more uncertain as no [SIII] was measured. Although the ratio seems to increase from knot A to D, the average error ( $\sim 0.18$ ) prevents us from drawing any conclusion about the homogeneity.

Regarding the logarithmic Ne/O ratio, knots A and C show the same value, -0.70, while for the rest of the knots the mean value is -0.94, with an average error of 0.07 dex for A and C and 0.20 dex for B, D, and E.

The Ar/O ratios found, in the range -2.28 to -2.06, show a very similar value for all knots, taking 0.17 dex as the average error (ranging from 0.09 up to 0.22 dex).

Finally, the derived helium abundances are the same for all five knots of NGC 6789 within observational errors, and similar to the values found for other BCDs (Izotov & Thuan 2004; Hägele et al. 2008).

## 5 CONCLUSIONS

In this paper, we present resolved stellar,  $H\alpha$ , and GALEX photometry, from different data archives, and WHT-ISIS optical spectroscopy of the five brightest star-forming knots of the nearest BCD galaxy NGC 6789 in order to study their SFH and metallicity.

The spectroscopic observations of NGC 6789 were taken using ISIS double-arm spectrograph attached to the 4.2m WHT, which allowed the simultaneous analysis of the spectra, covering from 3650 up to 7500 Å. From the long-slit spectra, we extracted and performed a detailed analysis of the five main star forming knots of the galaxy. Thanks to the measure of the [OIII] electron temperature in all knots and the measure of  $T([OII])$  in three of them, we provide “direct method” abundances for oxygen, nitrogen, sulphur, neon, and argon, not reported previously in the literature. Our analysis indicates that this galaxy is metal-poor ( $12 + \log(O/H)$  in the range 7.80 - 7.93) and chemically homogeneous, with quite similar values of the studied species in all knots. At same time, all the knots present values of  $N/O$  which are higher than expected for the metal regime of this galaxy.

We used optical data obtained from the HST archive to derive the SFH of NGC 6789 by means of the classical method of CMD reconstruction. We used the derived SFH in the program STARLIGHT to fit the optical spectrum and we compared these results with another non-constrained case. We corrected the emission-line measures from absorption and we derived the total stellar masses for each knot. Although the SFH obtained from the CMD is not foreseen by STARLIGHT in the non-constrained case, we checked that the total stellar mass and the ratio of older and younger stellar populations are not noticeably affected by the assumed SFH. Anyway, whenever possible, the extension of this type of studies for objects for which simultaneous resolved stellar photometry and optical spectroscopy are available will pro-

vide a much more accurate constrain to the age-metallicity-extinction degeneracy of these galaxies, as well as the comparison between nebular and stellar properties.

Finally, the ages and masses of the bursts of star formation in each knot were derived using CLOUDY tailored photoionisation models to fit the optical and UV photometric properties and the observed emission-line ratios and corrected  $H\beta$  equivalent widths. We found that dust absorption factors correlate much better with the GALEX FUV-NUV colour index than with the reddening constants derived from the Balmer decrement, indicating a very complex inner dust extinction structure. The models predict for all knots instantaneous bursts with ages in the range between 3 and 6 Myr. These ages do not follow any spatial trend in the galaxy image, so they are possibly related with the distribution of the galaxy in the line of sight. The dust absorption-corrected  $H\alpha$  fluxes were used to derive accurate SFRs for the individual knots.

The combination of several observational and model techniques lead to a better and auto-consistent study of NGC 6789. The derivation of a non-typical metallicity evolution using a CMD allows the use of the SFH to the subtraction of the older stellar population using spectral fitting to the optical spectrum with STARLIGHT. This information, together with the derivation of accurate physical properties and ionic chemical abundances pointing to similar low O/H and high N/O ratios in all knots allow the application of photoionisation models that predict dust-absorption factors fitting the GALEX colour indices and the derivation of ages (IBs in the range 3-6 Myr).

## ACKNOWLEDGEMENTS

R.G.B. acknowledges support from the China National Postdoc Fund Grant No. 20100480144 and MICINN AYA2010-15081. This work has been partially supported by DGI-CYT grant AYA2007-67965-C03, AYA2007-67965-C03-02, AYA2007-64712, and Junta de Andalucía TIC 114. The WHT is operated on the island of La Palma by the ING in the Spanish Observatorio del Roque de los Muchachos of the Instituto de Astrofísica de Canarias. We thank the Spanish allocation committee (CAT) for awarding observing time. We thanks We would like to thank to Armando Gil de Paz, for allowing the study of B, R, and  $H\alpha$  images of NGC 6789 in the Palomar/Las Campanas Atlas of Blue Compact Galaxies. We thank Roberto Cid Fernandes and the people of the STARLIGHT Project Team (UFSC, Brazil), for making the STARLIGHT code available. We acknowledge fruitful discussions with Enrique Pérez and Ricardo Amorín. We thank an anonymous referee for very useful comments that improved the presentation of the paper.

## REFERENCES

- Aloisi A., Tosi M., Greggio L., 1999, *AJ*, 118, 302  
 Anderson J., King I. R., 1999, *PASP*, 111, 1095  
 Aparicio A., Dalcanton J. J., Gallart C., Martinez-Delgado D., 1997, *AJ*, 114, 1447  
 Asplund M., Grevesse N., Sauval A. J., Scott P., 2009, *ARA&A*, 47, 481  
 Bergvall N., Östlin G., 2002, *A&A*, 390, 891  
 Brown T. M., Smith E., Ferguson H. C., Rich R. M., Guhathakurta P., Renzini A., Sweigart A. V., Kimble R. A., 2006, *ApJ*, 652, 323  
 Bruzual G., Charlot S., 2003, *MNRAS*, 344, 1000  
 Cairós L. M., Caon N., Zurita C., Kehrig C., Weilbacher P., Roth M., 2009, *A&A*, 507, 1291  
 Cardelli J. A., Clayton G. C., Mathis J. S., 1989, *ApJ*, 345, 245  
 Cerviño M., Luridiana V., 2006, *A&A*, 451, 475  
 Cerviño M., Valls-Gabaud D., 2003, *MNRAS*, 338, 481  
 Chabrier G., 2003, *PASP*, 115, 763  
 Cid Fernandes R., Gu Q., Melnick J., Terlevich E., Terlevich R., Kunth D., Rodrigues Lacerda R., Joguet B., 2004, *MNRAS*, 355, 273  
 Cid Fernandes R., Mateus A., Sodré L., Stasińska G., Gomes J. M., 2005, *MNRAS*, 358, 363  
 De Robertis M. M., Dufour R. J., Hunt R. W., 1987, *JRASC*, 81, 195  
 Diaz A. I., 1988, *MNRAS*, 231, 57  
 Díaz Á. I., 1998, *Ap&SS*, 263, 143  
 Dolphin A. E., 2000a, *PASP*, 112, 1397  
 Dolphin A. E., 2000b, *PASP*, 112, 1383  
 Dolphin A. E., 2002, *MNRAS*, 332, 91  
 Drozdovsky I., Tikhonov N., 2000, *A&AS*, 142, 347  
 Drozdovsky I. O., Schulte-Ladbeck R. E., Hopp U., Crone M. M., Greggio L., 2001, *ApJ*, 551, L135  
 Ferland G. J., Korista K. T., Verner D. A., Ferguson J. W., Kingdon J. B., Verner E. M., 1998, *PASP*, 110, 761  
 Filippenko A. V., 1982, *PASP*, 94, 715  
 García-Benito R., 2009, PhD thesis, Universidad Autónoma de Madrid  
 García-Benito R., Díaz A., Hägele G. F., Pérez-Montero E., López J., Vílchez J. M., Pérez E., Terlevich E., Terlevich R., Rosa-González D., 2010, *MNRAS*, 408, 2234  
 García-Benito R., Pérez E., Díaz Á. I., Maíz Apellániz J., Cerviño M., 2011, *AJ*, 141, 126  
 Garnett D. R., 1992, *AJ*, 103, 1330  
 Gil de Paz A., Madore B. F., Pevunova O., 2003, *ApJS*, 147, 29  
 Gonzalez-Delgado R. M., Perez E., Tenorio-Tagle G., Vilchez J. M., Terlevich E., Terlevich R., Telles E., Rodriguez-Espinosa J. M., Mas-Hesse M., Garcia-Vargas M. L., Diaz A. I., Cepa J., Castaneda H., 1994, *ApJ*, 437, 239  
 Hägele G. F., Díaz Á. I., Terlevich E., Terlevich R., Pérez-Montero E., Cardaci M. V., 2008, *MNRAS*, 383, 209  
 Hägele G. F., García-Benito R., Pérez-Montero E., Díaz Á. I., Cardaci M. V., Firpo V., Terlevich E., Terlevich R., 2011, *MNRAS*, 414, 272  
 Hägele G. F., Pérez-Montero E., Díaz Á. I., Terlevich E., Terlevich R., 2006, *MNRAS*, 372, 293  
 Harris J., Zaritsky D., 2001, *ApJS*, 136, 25  
 Harris J., Zaritsky D., 2004, *AJ*, 127, 1531  
 Harris J., Zaritsky D., 2009, *AJ*, 138, 1243  
 Hernandez X., Gilmore G., Valls-Gabaud D., 2000, *MNRAS*, 317, 831  
 Holtzman J. A., Hester J. J., Casertano S., Trauger J. T., Watson A. M., Ballester G. E., et al. 1995, *PASP*, 107, 156  
 Hopkins A. M., Schulte-Ladbeck R. E., Drozdovsky I. O., 2002, *AJ*, 124, 862



- Inoue A. K., 2001, *AJ*, 122, 1788
- Izotov Y. I., Thuan T. X., 1999, *ApJ*, 511, 639
- Izotov Y. I., Thuan T. X., 2004, *ApJ*, 602, 200
- Karachentsev I. D., Makarov D. I., 1998, *A&A*, 331, 891
- Kehrig C., Vílchez J. M., Sánchez S. F., Telles E., Pérez-Montero E., Martín-Gordón D., 2008, *A&A*, 477, 813
- Kennicutt Jr. R. C., 1998, *ARA&A*, 36, 189
- Kennicutt Jr. R. C., Bresolin F., Garnett D. R., 2003, *ApJ*, 591, 801
- Kingdon J., Ferland G. J., 1995, *ApJ*, 442, 714
- Köppen J., Hensler G., 2005, *A&A*, 434, 531
- Krist J., 1995, in Shaw R. A., Payne H. E., Hayes J. J. E., eds, *Astronomical Data Analysis Software and Systems IV* Vol. 77 of *Astronomical Society of the Pacific Conference Series*, Simulation of HST PSFs using Tiny Tim. p. 349
- Kroupa P., 2002, *Science*, 295, 82
- Kunth D., Sargent W. L. W., 1983, *ApJ*, 273, 81
- Le Borgne J.-F., Bruzual G., Pelló R., Lançon A., Rocca-Volmerange B., Sanahuja B., Schaerer D., Soubiran C., Vílchez-Gómez R., 2003, *A&A*, 402, 433
- Leitherer C., Robert C., Drissen L., 1992, *ApJ*, 401, 596
- Leitherer C., Schaerer D., Goldader J. D., Delgado R. M. G., Robert C., Kune D. F., de Mello D. F., Devost D., Heckman T. M., 1999, *ApJS*, 123, 3
- Leroy A., Bolatto A. D., Simon J. D., Blitz L., 2005, *ApJ*, 625, 763
- Liu X.-W., Storey P. J., Barlow M. J., Danziger I. J., Cohen M., Bryce M., 2000, *MNRAS*, 312, 585
- Loose H.-H., Thuan T. X., 1986, *ApJ*, 309, 59
- Magrini L., Bianchi S., Corbelli E., Cortese L., Hunt L., Smith M., Vlahakis C., Davies J., Bendo G. J., Baes M., Boselli A., Clemens M., et al. 2011, *A&A*, 535, A13
- Marigo P., Girardi L., Bressan A., Groenewegen M. A. T., Silva L., Granato G. L., 2008, *A&A*, 482, 883
- Martin D. C., Fanson J., Schiminovich D., Morrissey P., Friedman P. G., Barlow T. A., Conrow T., Grange R., Jelinsky P. N., Milliard B., et al. 2005, *ApJ*, 619, L1
- Mateus A., Sodr   L., Cid Fernandes R., Stasi  nska G., Schoenell W., Gomes J. M., 2006, *MNRAS*, 370, 721
- Matteucci F., Chiosi C., 1983, *A&A*, 123, 121
- Meynet G., Maeder A., Schaller G., Schaerer D., Charbonnel C., 1994, *A&AS*, 103, 97
- Moll   M., V  lchez J. M., Gavil  n M., D  az A. I., 2006, *MNRAS*, 372, 1069
- Morrissey P., Schiminovich D., Barlow T. A., Martin D. C., Blakkolb B., Conrow T., Cooke B., Erickson K., Fanson J., Friedman P. G., Grange R., Jelinsky P. N., et al. 2005, *ApJ*, 619, L7
- Olive K. A., Skillman E. D., 2001, *New Astronomy*, 6, 119
- Osterbrock D. E., 1989, *Astrophysics of Gaseous Nebulae and Active Galactic Nuclei*. University Science Books
-   stlin G., 2000, *ApJ*, 535, L99
- Ot  -Floranes H., Mas-Hesse J. M., 2010, *A&A*, 511, A61+
- Papaderos P., Izotov Y. I., Guseva N. G., Thuan T. X., Fricke K. J., 2006, *A&A*, 454, 119
- Papaderos P., Loose H.-H., Thuan T. X., Fricke K. J., 1996, *A&AS*, 120, 207
- Peimbert M., Costero R., 1969, *Bolet  n de los Observatorios Tonantzintla y Tacubaya*, 5, 3
- P  rez-Montero E., Contini T., 2009, *MNRAS*, 398, 949
- P  rez-Montero E., D  az A. I., 2003, *MNRAS*, 346, 105
- P  rez-Montero E., D  az   . I., 2007, *MNRAS*, 377, 1195
- P  rez-Montero E., Garc  a-Benito R., D  az A. I., P  rez E., Kehrig C., 2009, *A&A*, 497, 53
- P  rez-Montero E., Garc  a-Benito R., H  gele G. F., D  az   . I., 2010, *MNRAS*, 404, 2037
- P  rez-Montero E., V  lchez J. M., Cedr  s B., H  gele G. F., Moll   M., Kehrig C., D  az A. I., Garc  a-Benito R., Mart  n-Gord  n D., 2011, *ArXiv e-prints*
- Pflamm-Altenburg J., Weidner C., Kroupa P., 2007, *ApJ*, 671, 1550
- Pflamm-Altenburg J., Weidner C., Kroupa P., 2009, *MNRAS*, 395, 394
- Rela  o M., Kennicutt R. C., 2009, *ApJ*, 699, 1125
- Salpeter E. E., 1955, *ApJ*, 121, 161
- Sargent W. L. W., Searle L., 1970, *ApJ*, 162, L155+
- Schlegel D. J., Finkbeiner D. P., Davis M., 1998, *ApJ*, 500, 525
- Shaklan S., Sharman M. C., Pravdo S. H., 1995, *Appl. Opt.*, 34, 6672
- Shaw R. A., Dufour R. J., 1995, *PASP*, 107, 896
- Smith L. J., Norris R. P. F., Crowther P. A., 2002, *MNRAS*, 337, 1309
- Smits D. P., 1996, *MNRAS*, 278, 683
- Storey P. J., Hummer D. G., 1995, *MNRAS*, 272, 41
- Tolstoy E., Hill V., Tosi M., 2009, *ARA&A*, 47, 371
- van Zee L., Haynes M. P., 2006, *ApJ*, 636, 214
- V  zquez G. A., Leitherer C., 2005, *ApJ*, 621, 695
- Vila Costas M. B., Edmunds M. G., 1993, *MNRAS*, 265, 199
- V  lchez J. M., Iglesias-P  ramo J., 2003, *ApJS*, 145, 225
- Williams B. F., Ciardullo R., Durrell P. R., Vinciguerra M., Feldmeier J. J., Jacoby G. H., Sigurdsson S., von Hippel T., Ferguson H. C., Tanvir N. R., Arnaboldi M., Gerhard O., Aguerri J. A. L., Freeman K., 2007, *ApJ*, 656, 756
- Zhao Y., Gu Q., Gao Y., 2011, *AJ*, 141, 68